Doctoral Thesis

Study on Electrostatic Force Generation and Position Feedback Control for High Performance of Electrostatically Controlled Linear Actuator

March, 2015

Doctoral Program In Integrated Science and Engineering
Graduate School of Science and Engineering
Ritsumeikan University

NGUYEN ANH TUAN

Doctoral Thesis reviewed
by Ritsumeikan University

Study on Electrostatic Force Generation and Position Feedback Control for High Performance of Electrostatically Controlled Linear Actuator

(静電制御型リニアアクチュエータの高性能化のための
静電力発生とフィードバック位置制御に関する研究)

March, 2015
2015 年 3 月

Doctoral Program In Integrated Science and Engineering
Graduate School of Science and Engineering
Ritsumeikan University
立命館大学大学院理工学研究科
総合理工学専攻博士課程後期課程

NGUYEN ANH TUAN
ぐえん　あん　ちゅあん

Supervisor: Professor SATOSHI KONISHI
研究指導教員：小西 聡 教授

CONTENTS

ACKNOWLEDGEMENTS

I would like to express my sincerest gratitude to my supervisor Professor Satoshi Konishi, who has been a tremendous mentor for me. I would like to thank you for encouraging my research and for allowing me to grow as a research scientist. Without your valuable advice, guidance, and enthusiasm, there would be no this thesis today. I would like to thank Professor Toshiyuki Toriyama and Professor Satoshi Ueno for co-examining and reviewing this dissertation. I would also like to thank Professor Taeko Ando for her kind advice and helpful suggestions in research.

My appreciation goes to Dr. Wataru Tonomura and Dr. Taizo Kobayashi for their helps and expert advice. Konishi laboratory is a great place to work because of the friendly people and professional research environment. I would like to show my gratitude to all members of our laboratory: Dr. Koji Hattori, Mrs. Tsubasa Matsuyama, Masatoshi Ito, Kuwamura Tomuki, Kazuki Ishi, Naoyuki Igata, Yuta Nakanishi, etc. for helping and sharing me the wonderful working and living experiences in Japan. I would also like to thank my Vietnamese friends for sharing with my life in Japan.

Special thanks to my family. Words cannot express how grateful I am to my grandfather, grandmother, my parent in-law, and my mother for all of the sacrifices that you have made on my behalf. I would like to give special thanks from my heart to my father in the heaven. I miss you so much, Dad. To my beloved wife, Nguyen Thu Ha, I do not know how to express my thanks to you. However, I know that you are a wonderful wife. I have realized that no matter how hard life gets and whatever happens, you always give me a reliable love. You have tried your best to take care of our babies. My daughter and son, you are really my angels. I wish you know that how much I love you. Thank you all for giving me a tremendous power.

Finally, I would also like to thank the Vietnamese Government Scholarship Program for financial supports during my studies at Ritsumeikan University.

ABSTRACT

This thesis studies on the electrostatic force generation and position feedback control for high performance of an electrostatically controlled linear actuator (ECLIA). The ECLIA consisting of a piezoactuator (PZT), driving and holding electrodes, and sliders provides precise motion and large stroke. In literature, novel technologies have been studied for improvements of the actuator. Among these, a micro-potentiometer using a probe dipped in μpool (PDP) was proposed and employed to detect position of the slider. As a development stage, this thesis reports on the following issues aiming higher performance of the ECLIA: (1) Introducing a flexible electrode with a sandwich structure for higher electrostatic-force generation, (2) Increasing the pushing force using a fishbone structure mounted on the flexible slider, and (3) Position feedback control using a micro-potentiometer and microcontroller.

This thesis consists of six chapters. The first chapter introduces the background, and objective of the study. In chapter 2, the structure and working principle of the ECLIA are described. Chapter 3 presents the flexible electrode having a conductive layer sandwiched between insulating layers. The flexible electrode could deform and fit to the contact electrode for higher efficiency of electrostatic-force generation. Therefore, the flexible electrode exhibited a significant improvement in the electrostatic clutching force in comparison with the Si electrode. In chapter 4, a design of the fishbone structure for improving the longitudinal stiffness of the flexible slider is presented. The fishbone slider showed a higher performance in terms of the pushing force than that of the Si slider. Chapter 5 describes the design and implementation of a position feedback controller using a micro-potentiometer and a microcontroller. It was indicated that the feedback control with tuning gains performed a significant improvement compared to that without tuning gains. The final chapter summarizes this thesis.

LIST OF TABLES

LIST OF FIGURES

Chapter 1

INTRODUCTION

1.1. Research background

Micro-actuators have been widely used in microelectromechanical systems (MEMS) fields. The actuators are operated by using different actuating principles such as electrostatic [1–3], thermal [4,5], piezoelectric [6–9], magnetic [10–12], and pneumatic actuations [13–15]. A piezoelectric actuator can provide precise motion and a large force. Actuators based on electrostatic effect generate a small displacement. However, electrostatically controlled stepwise motion can convert short-range actuation into long-range travel/ large stroke. Actuators using a stepwise motion method present precise motion and a large stroke for micro-system applications [6,16]. A high-precision positioning technology has played an important role in engineering fields such as optical positioning, biomedical manipulation, etc. [17–20]. Various types of MEMS actuators are being used as a positioner with high accuracy [16,21–23]. In addition, a large travel range is also important for tracking in a wide area [24].

An electrostatically controlled linear actuator (ECLIA) has been proposed and developed at the Konishi laboratory in order to obtain parallel, precise motion, a large stroke and force generation [6]. The ECLIA comprises a PZT actuator, multiple sliders, driving and holding electrodes. A driving control system generates control signals for the ECLIA. The working principle of the ECLIA utilizes the stepwise motion that is driven by the PZT actuator combined with an electrostatic clutch mechanism. The PZT expands and pushes the driving electrode that carries the slider by/using the electrostatic clutch mechanism. The PZT actuator provides a fine motion in the order of nanometers; the electrostatic clutch mechanism is formed by applying electrical signal to the driving, holding electrodes and sliders independently. Consequently, the ECLIA can be applied for an optical dynamics gain equalizer (DGEQ) to distribute optical attenuation for wavelength division multiplexing (WDM) signals [25], micro-syringe pumps for picoliter-scale liquid manipulation [26], micro-grippers, etc.

An output force is an important factor of MEMS actuators. The output force was required to exert external objects for micro transportation systems or gripper applications [27,28]. A micro-gripper using electrostatic actuation produced a grasping force of 3 mN for optical fiber and transporting polymer objects [28]. The electrostatic actuators using inchworm motion reported a pushing force of ±0.45 mN [2]. In the micro-syringe pumps application of the ECLIA, the pushing force was estimated as 3.85 mN [26]. In the ECLIA, the PZT expands and pushes the driving electrode together with the slider using the electrostatic clutch mechanism. The pushing force of the slider is transmitted by the generated force from the PZT actuator combined with the electrostatic clutch mechanism. The non-coplanar of the PZT and the driving electrode causes the bending deformation of the driving electrode. This deformation creates a larger air gap between the Si slider and the driving/holding electrodes. The air gap decreases the electrostatic clutching force, and thus reduces the pushing force of the slider. The relative sliding of the electrostatic clutch mechanism also reduces the precision of position control. Hence, the pushing force and position control of the ECLIA need to be improved.

In recent years, polymeric material has been widely used in MEMS field due to the simple and low-cost process compared to Si. A flexible electrode that is made by a conductive polymer coated on a polymeric thin film was proposed by Ito and Konishi [29]. The flexible electrode can deform and fit to the opposite electrode in order to reduce the air gap and to improve electrostatic-force generation for the ECLIA. A probe dipped in μpool (PDP) connection was proposed at Konishi laboratory [30]. The PDP connection uses a probe to supply electrical signal for a moving object through a μpool filled with ionic liquid. Hence, the moving object has only the physical resistance of liquid. This PDP connection overcomes the mechanical restriction comparing to a conventional wiring connection. A micro-potentiometer using PDP technology was also developed for detecting position of the slider with low physical restriction and resolution in micro-meter range [31]. The micro-potentiometer mounted on a slider is utilized to detect the slider displacement. This is an important factor for the next step in control aspect of the ECLIA. Microcontrollers with attractive characteristics such as compactness, mobility, and familiar programing languages have been employed in control systems [32,33]. A microcontroller computes and generates control signals for the ECLIA. Proportional–integral–derivative (PID) controllers have been commonly used in many feedback control systems owing to their simple structure and adaptability [34–36]. The PID controller has three control parameters called proportional, integral and derivative gains (K_p, K_i and K_d). In order to trade-off between financial efficiency

and acceptable overall quality, many applications require only one or two control parameters to provide the appropriate control system. The PI, PD or P controller is chosen depending on the specific system and desired operation.

1.2. Research purposes

As mentioned in previous section, the ECLIA has attractive characteristics such as parallel, precise motion, and a large stroke for applications such as micro-syringe pumps, an optical DGEQ, etc. Nevertheless, the larger air gap due to the bending deformation of the driving electrode reduces the clutching force and thus causes reduction in the pushing force. Reducing the air gap is an important issue to obtain the higher pushing force. The relative sliding of the electrostatic clutching mechanism also causes inequality of the stepwise motion, this results the difficulty in determination of the slider displacement. Using the position sensor and feedback control can improve position control of the ECLIA. As our development stage, this dissertation focuses on improving the pushing force by reducing the air gap. We also consider the position feedback control to achieve higher performance for the ECLIA.

The flexible slider can deform and fit to the opposite electrode to reduce the air gap for having efficient electrostatic-force generation. However, the flexible slider has a low longitudinal stiffness and a small buckling force (0.03 mN). An increase in the longitudinal stiffness of the flexible slider needs to be improved to enhance the pushing force. In previous study, a flexible electrode with a conductive polymer coated on a polymer base film was proposed by Ito and Konishi [29]. A backbone structure was proposed to improve the longitudinal stiffness of a thin film Si slider by Saika [37]. In this research, we present a polymer slider that comprises a conductive layer sandwiched between insulating layers. The bottom insulating layer is fabricated in thin thickness for efficient electrostatic-force generation. A slider consisting of the fishbone structure mounted on the flexible polymer film is proposed to enhance the pushing force. The fishbone structure only occupies a small area of the slider surface; therefore, the fishbone structure has a minor reduction in the flexibility of the slider. The fishbone slider is expected to obtain higher performance of pushing-force generation.

A position control is required for ECLIA applications. We propose a position feedback control utilizing a micro-potentiometer and microcontroller. The micro-potentiometer mounted on the slider allows detecting the slider displacement without mechanical binding. The control parameters are tuned and investigated to choose their

optimal values. The position feedback control aims to reduce control time, overshoot, oscillation, and steady-state error for higher performance of ECLIA applications.

Chapter 2

ELECTROSTATICALLY CONTROLLED LINEAR ACTUATOR

2.1. Overview

This chapter introduces the configuration, working principle, and stepwise motion characteristics of an electrostatically controlled linear actuator (ECLIA). The stepwise motion, which is produced by the PZT actuation combined with an electrostatic clutch mechanism, allows parallel, precise motion, and a large stroke of sliders. The bending deformation of the driving electrode creates an air gap between the slider and the electrodes. A slider and a contact electrode with an insulating layer form a capacitor. If the thickness of the insulating layer decreases, the capacitance increases, and therefore the electrostatic-force generation will be improved for higher electrostatic clutching force. This aims an improvement of the pushing force. We will consider the capacitance, electrostatic clutching force and pushing force in this chapter. Furthermore, the inequality of the stepwise motion caused by the relative sliding of the electrostatic clutch mechanism is also evaluated using a dynamic model of the ECLIA.

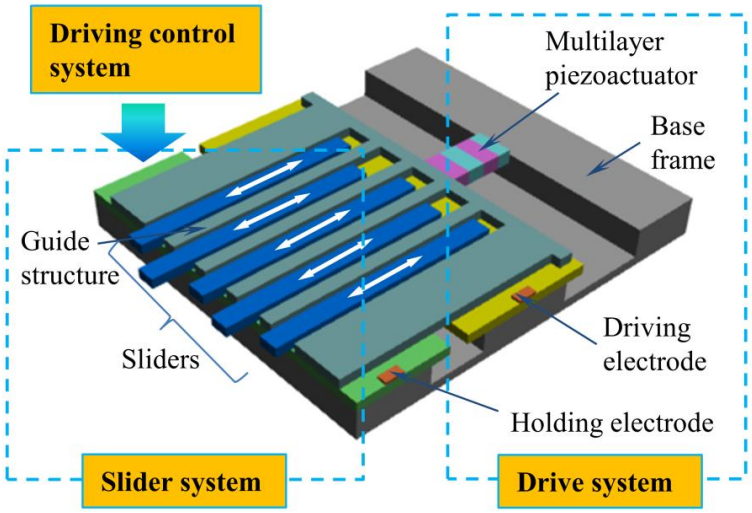

Figure 2.1. Schematic diagram of the ECLIA [6].

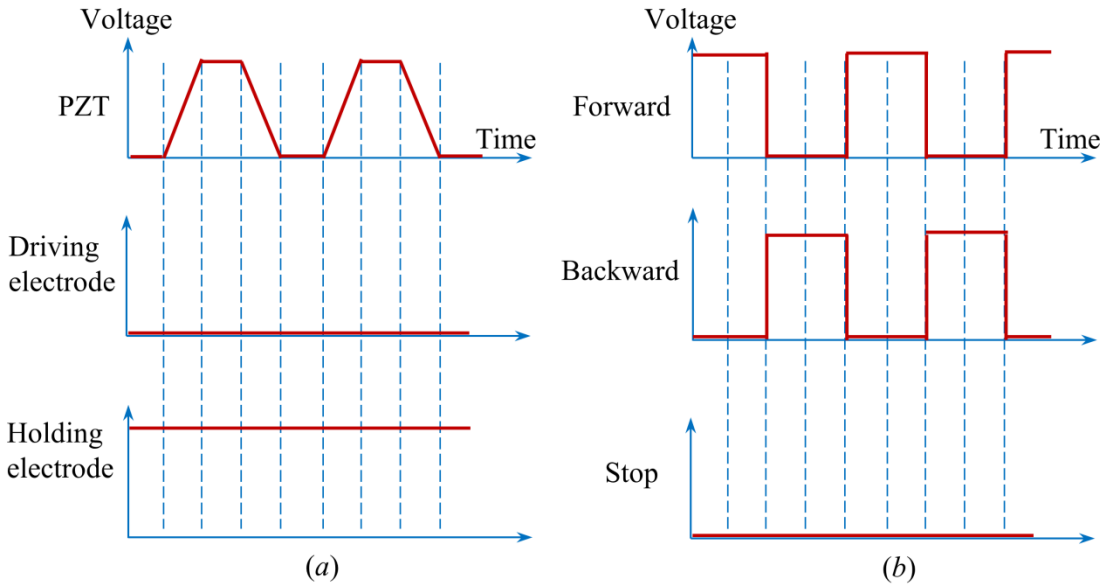

Figure 2.2. Drive control signals of the ECLIA for: (*a*) Drive system and (*b*) slider system [6].

2.2. System configuration

Figure 2.1 shows the composition of the ECLIA that consists of the drive, slider, and driving control systems. The drive system comprises a PZT actuator, driving and holding electrodes. The driving electrode is supported by a double parallel beams hinge at the side edges. The PZT actuator is mounted on a base frame at one end, and the other is tied with the driving electrode using an epoxy resin. The holding electrode is fixed to the base frame. The slider system comprises multiple sliders which are arranged in parallel on the driving and holding electrodes. An insulating layer isolates electrical signal between each slider and the electrodes. A guide structure employs sliders in their straight motion. The driving control system generates control signals to the ECLIA. The electrical signals supply to the slider and electrodes to produce an electrostatic clutching force and thus to form an electrostatic clutch mechanism. The PZT actuator, sliders, driving and holding electrodes are supplied appropriate electrical signals to operate multiple sliders independently. The working principle of ELCIA will be described in the following section.

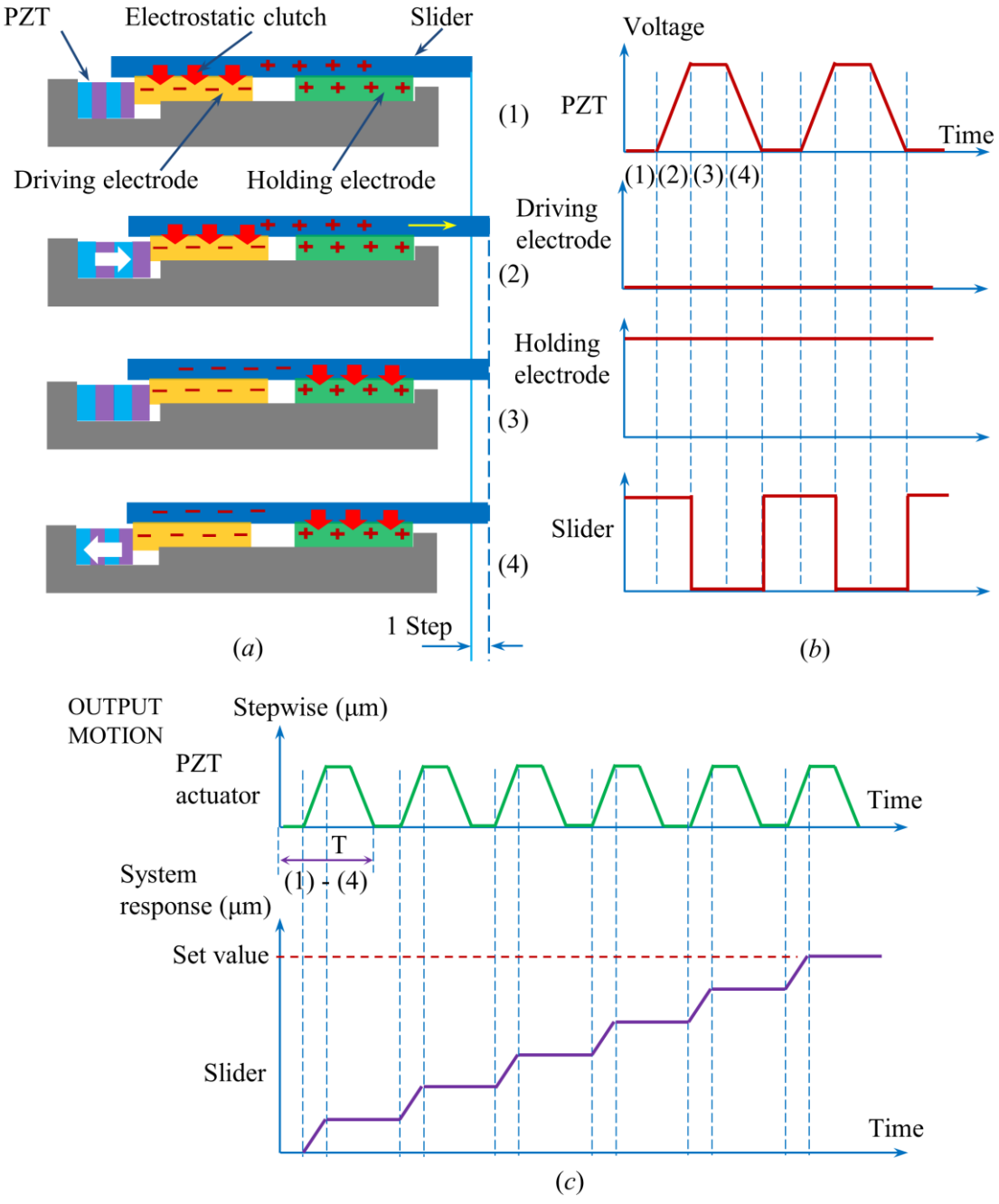

Figure 2.3. ECLIA: (*a*) cross section, (*b*) wave form of drive control signal for forward motion of the slider, and (*c*) output motion of the actuator [6].

2.3. Working principle

This section describes the detail of electrical forms that are employed for the ECLIA to yield the stepwise motion of the sliders. The electrostatic clutching force creates the

electrostatic clutch mechanism between the slider and the driving/holding electrodes. The stepwise motion of the slider is operated by the PZT actuator and the electrostatic clutch mechanism. Wave forms of the control signals introducing to the ECLIA are shown in Figure 2.2. Figure 2.2(*a*) describes the pattern of electrical signals applied to the driving system (the PZT actuator, driving and holding electrodes). The forms of electrical signals supplied to a slider for the forward, backward motion and stop are shown in Figure 2.2(*b*). Moreover, every slider is isolated electrical signal to each other that can be possible to drive multiple sliders in parallel motion. To describe the working principle of the ECLIA, an example in forward motion of the slider is presented.

Figure 2.3(*a*) shows a cross section of the ECLIA corresponding to an example of electrical signals (Figure 2.3(*b*)) that are supplied to the PZT actuator, the driving, holding electrodes, and the slider. One step forward motion of the slider can be divided into four steps:

(1) The electrostatic clutch mechanism is yielded between the slider and the driving electrode owing to the different sign of electrical signals.

(2) The PZT actuator expands at the rising edge of the supplied signal to push the driving electrode together with the slider moving forward a step.

(3) The drive signal of the slider is switched to a negative value such that the slider releases the suction with the driving electrode and grasps to the holding electrode.

(4) The PZT actuator shrinks at the falling edge of the signal and thus pulls the driving electrode to the initial position. In the meanwhile, the slider is still grasped to the holding electrode.

A large displacement of the slider can be obtained by repeating steps (1) through (4) as many times as necessary (Figure 2.3(*c*)).

2.4. Electrostatic clutch mechanism

2.4.1. Capacitance

A capacitor is formed by the slider with an insulating layer and the driving/holding electrode. Additionally, the bending deformation of driving electrode creates an air gap between the slider and the electrode (see Figure 2.4(*a*)). Consequently, they can be

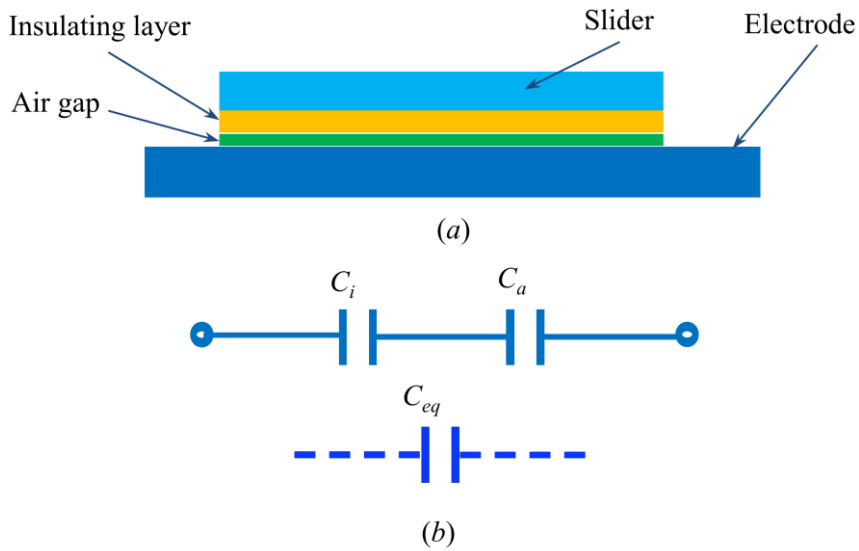

Figure 2.4. Schematic diagram of (*a*) the slider and the opposite electrode, and (*b*) an equivalent capacitor.

expressed by the series capacitors C_i (insulating layer) and C_a (air gap) as shown in Figure 2.4(*b*). The equivalent capacitance C_{eq} is calculated using

$$C_{eq} = \frac{C_i C_a}{C_i + C_a} \tag{2.1}$$

The theoretical capacitance C between two parallel electrodes with a dielectric layer is well known as

$$C = A\frac{\varepsilon}{d} \tag{2.2}$$

where A is the overlap area of the two electrodes, and ε and d are the permittivity and thickness of the dielectric layer, respectively.

If the thickness of the insulating layer and air gap decrease, the capacitance increases.

2.4.2. Electrostatic clutching force

When a voltage is applied to the slider and electrode, the electrostatic force is generated and thus producing the electrostatic clutching force (see Figure 2.5). This clutching

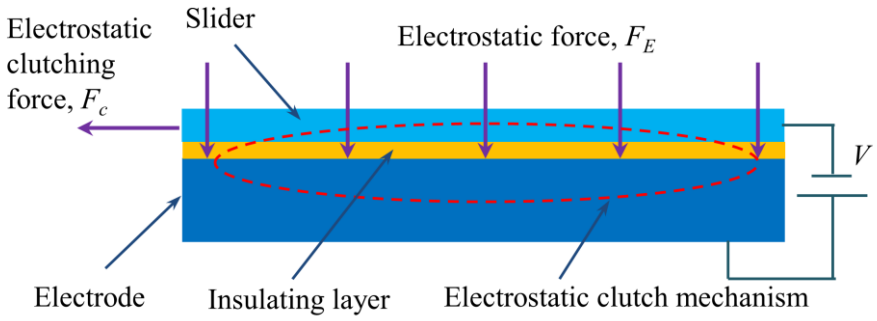

Figure 2.5. Electrostatic clutching force between the slider and the opposite electrode.

force forms the electrostatic clutch mechanism between the slider and the electrode. The electrostatic force F_E is calculated using

$$F_E = -\frac{A\varepsilon}{2d^2}V^2 \tag{2.3}$$

where V is the applied voltage.

The electrostatic clutching force F_c is defined as

$$F_c = \mu F_E \tag{2.4}$$

where μ is the frictional coefficient between the slider and the electrode.

If the insulating layer and air gap decrease, the electrostatic clutching force will increase. In this research, we propose a method to reduce the insulating layer and air gap for improving the performance of the ECLIA in term of the electrostatic-force generation. Figure 2.6 shows the apparatus for measuring the electrostatic clutching force using a load cell (KYOWA, LVS-200GA, Japan). A driving voltage is applied to the slider and Si electrode by a dc voltage source.

2.5. Characteristics of stepping actuation

Previous section describes the structure and characteristics of the electrostatic clutch mechanism. This clutch mechanism causes a relative sliding between the slider and the opposite electrode, resulting in inequality of the stepwise motion. In this section, the ECLIA is modeled to investigate these features of the stepping actuation.

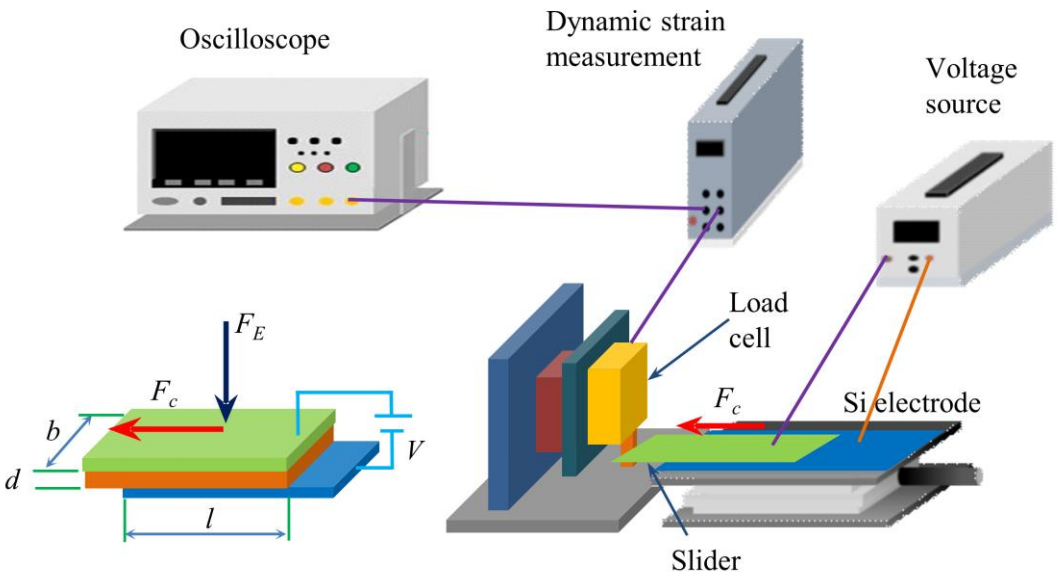

Figure 2.6. Apparatus for measuring the electrostatic clutching force (F_c).

Figure 2.7(*a*) shows a cross section of the ECLIA. The driving electrode supported by a double layer parallel beam hinges is directly driven by the PZT actuator (see Figure 2.7(*b*), top view). According to the schematic in Figure 2.7(*b*), a model of the driving system is shown in Figure 2.7(*c*). The PZT actuator can be described as a spring model with stiffness k_a. The multiple parallel beams can be modeled as a spring with stiffness k_b, and a damper with damping constant *d*. The driving electrode mass is denoted as *m*. The input displacement of the driving electrode *x* is the output displacement of the PZT actuator. The output displacement of the driving electrode and the slider are *y* and *z*, respectively. The instability of electrostatic clutch mechanism that causes an undesired sliding between the slider and the driving, holding electrodes can be expressed as a sliding coefficient, λ (≤ 1) in this research. The force-balance equation can be deduced as below

$$m\ddot{y} + d\dot{y} + (k_b + k_a)y = k_a x \tag{2.5}$$

$$z = \lambda y \tag{2.6}$$

Using Laplace transform with initial conditions: $y(0) = 0$ and $\dot{y}(0) = 0$, the solution of (2.5) is deduced as follows:

$$y(t) = \frac{k_a}{k_a + k_b} x(t) \tag{2.7}$$

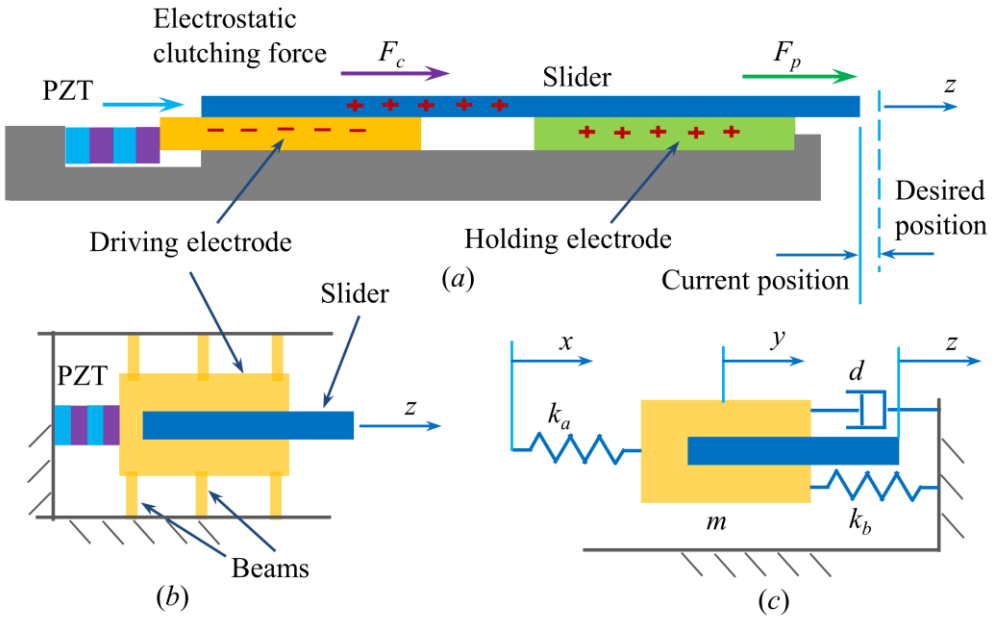

Figure 2.7. ECLIA: (*a*) cross section, (*b*) schematic diagram in top view and (*c*) model of the driving system.

Substituting (2.7) into (2.6), we obtain

$$z(t) = \lambda \frac{k_a}{k_a + k_b} x(t) \tag{2.8}$$

The deformation of a cantilever beam δ can be expressed as [38]

$$\delta = \frac{PL^3}{3EI} = \frac{4PL^3}{Ebh^3} \tag{2.9}$$

where P is the force exerted on the beam; E is the material elastic modulus, and L, b and h are the length, width and height of the beam, respectively.

Then, the spring stiffness of n parallel beams can be given as

$$k_b = n\frac{P}{\delta} = n\frac{Ebh^3}{4L^3} \tag{2.10}$$

Table 2.1. Parameters of the ECLIA.

***m* (kg)**	***L* (m)**	***b* (m)**	***h* (m)**	***n***	***E* (N m^{-2})**	***k*$_a$ (N m^{-1})**
1.01×10^{-4}	0.0005	0.0001	0.0002	18	165×10^{9}	22×10^{6}

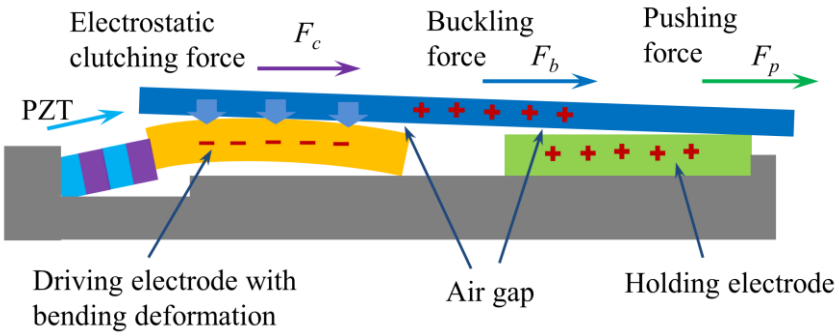

Figure 2.8. Schematic diagram of the ECLIA with force generation.

The parameters of the ECLIA are summarized in Table 2.1. Substituting the determined values into (2.10), we calculate k_b = 4.752×10^6 N m^{-1}. Hence, the stepping motion of the slider with respect to the output motion of the PZT is shown as follows:

$$z(t) = 0.822\lambda x(t) \tag{2.11}$$

This equation indicates that the stepwise motion of the slider z is smaller than the output motion of the PZT actuator x. In addition, the inherent hysteresis and creep behaviors of the PZT actuator cause inequality in stepping motion of the slider at different driving frequencies. The stepwise motion also depends on the relative sliding characteristic of the electrostatic clutch mechanism. The sliding coefficient λ is variable in each stepping motion, and thus the stepping displacement of the slider varies in each step. Therefore, it is difficult to calculate the displacement of the slider on the basis of the number of steps. The position sensor and feedback control will be considered to overcome this challenge.

2.6. Pushing force

The PZT actuator is bonded directly with the driving electrode using an epoxy resin. It is difficult to adjust the PZT actuator and the electrode in coplanar. This causes the bending deformation of the driving electrode when the PZT expands and pushes the electrode moving forward as shown in Figure 2.8. This bending phenomenon produces a larger air gap between the slider and the electrodes. The air gap reduces the electrostatic force and the electrostatic clutching force.

The ECLIA provides the pushing force F_p that is transmitted from the PZT actuator based on the electrostatic clutch mechanism (see Figure 2.8). The slider should not be buckled when applying the pushing force. It means that the pushing force should

be smaller than the buckling force of the slider F_b. The electrostatic clutch mechanism occurs the relative sliding when the pushing force is larger than the clutching force F_c. The generated force from the PZT (max 200 N, PZT actuator AE0203D08F, NEC Corporation, Japan) is much larger than the electrostatic clutching force and the buckling one (in the range of mN). If the buckling force is larger than the clutching force ($F_b > F_c$), the pushing force cannot exceed the clutching force ($F_p \leq F_c$) due to the relative sliding of the clutch mechanism. In the contrast, if the buckling force is smaller than the clutching force ($F_b < F_c$), the pushing force cannot exceed the buckling force ($F_p \leq F_b$) because of the buckling phenomenon of the slider. The maximum value of the pushing force F_{p_max} can be determined as

$$F_{p\_\max} = \min(F_b, F_c) \tag{2.12}$$

or

$$F_{p\_\max} = kF_b + (1-k)F_c \tag{2.13}$$

where, $k = 1$ if $F_b < F_c$; $k = 0$ if $F_b > F_c$

2.7. Summary and discussion

In this chapter, we have presented the configuration, working principle, and stepwise motion characteristics of the ECLIA. The ECLIA can achieve parallel motion with nanometer order accuracy and millimeter order stroke of multiple sliders. The stepwise motion of the slider manipulated by the PZT actuator combined with the electrostatic clutch mechanism was evaluated using a dynamic model of the ECLIA. According to (2.2) and (2.3), a smaller air gap corresponds to a higher capacitance and a larger electrostatic force, and thus the electrostatic clutching force is larger. The bending deformation of the driving electrode produces a larger air gap. This causes the reduction in the pushing force of the slider. In the following chapter, the flexible electrode is mentioned for higher efficiency of electrostatic-force generation.

Chapter 3

FLEXIBLE ELECTRODE FOR EFFICIENT ELECTROSTATIC-FORCE GENERATION

3.1. Overview

This chapter proposes a flexible electrode with sandwich structure for higher efficiency of electrostatic-force generation for ECLIAs. As mentioned in the previous chapter, an insulating layer and undesired air gap decrease the electrostatic-force generation. The hard contact surfaces of Si bulk electrodes create a larger air gap because of the bending deformation of the driving electrode. It is important to reduce the air gap for improving performance in force generation of the actuator. Thus, the flexible electrode, which can deform and fit to the opposite electrode, is proposed for this purpose.

The thickness of the flexible electrode is also an important factor. The thinner electrode requires the lower driven voltage, but it has challenges such as warping and high sticking phenomena. Hence, the requirement of the flexible electrode is enough thickness while remaining low applied voltage. The flexible electrode, which comprises a conductive layer sandwiched between two insulating layers, is proposed to satisfy the above requirement. The fabrication method, production results and characteristics of the flexible electrode will be described in this chapter. This flexible electrode can be served as the flexible slider for high performance in force generation aspect of the ECLIA.

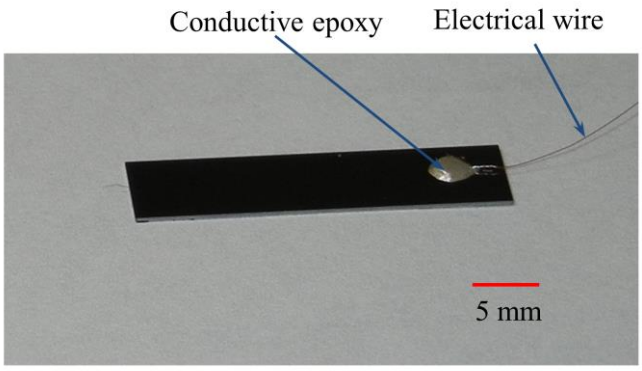

Figure 3.1. Image of the Si electrode.

3.2. Conventional rigid electrode

In this section, we describe and compare the physical features of a Si bulk electrode and a flexible one. The rigid electrode was fabricated using a Si wafer with a 150 μm thickness in this research. The rectangular shape (25 mm length and 5 mm width) of the Si bulk electrode was diced using a dicing machine (DAD 522, DISCO Corporation, Japan). A 1 μm thick insulating parylene layer was formed using a specialty coating systems (Rabokota PDS 2010, SCS, America) for this investigation. Additionally, a Cu wire (0.2 mm diameter) was bonded using a conductive epoxy to supply electrical signal

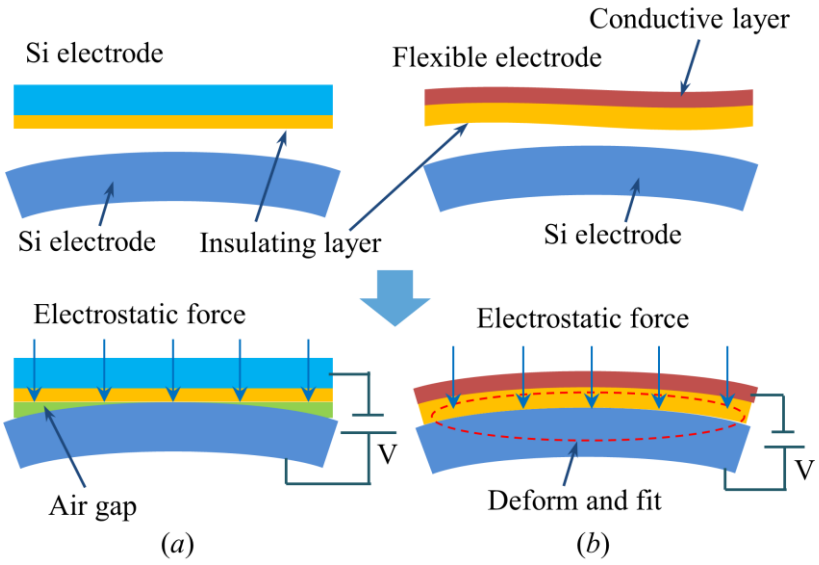

Figure 3.2. Schematic diagram of (*a*) the Si electrode and (*b*) the flexible one contact to the Si electrodes.

to the electrode. Figure 3.1 shows the fabricated Si electrode.

As previously discussed, the air gap causes a reduction in the electrostatic force. The bending deformation of the driving electrode creates a large air gap between two Si electrodes (see Figure 3.2(*a*)). In this research, the flexible electrode that can deform and fit to the contact electrode is proposed in order to reduce the air gap, and thus improves the efficient electrostatic-force generation (Figure 3.2(*b*)). The physical features of the Si bulk and flexible electrodes are listed and compared in Table 3.1.

3.3. Design of flexible electrode

In this section, we mention a flexible electrode [29] with the design that comprises a conductive polymer layer sandwiched between two insulating layers. The properties of different conductive and insulating polymers are evaluated to optimize the selection of materials for the flexible electrode. We also consider the fabrication method, warping and sticking phenomena of the flexible electrode.

The flexible electrode can obtain a better fit to the contact electrode under the electrostatic clutching force. A simple flexible electrode consists of an insulating layer and a conductive layer as shown in Figure 3.2(*b*). If the electrode is thinner, it has more flexibility and requires the lower applied voltage for electrostatic-force generation. However, a thin electrode has drawbacks in fabrication, difficulty in moving due to low longitudinal stiffness and sticking with the contact surface. To overcome the mentioned

Table 3.1. Physical features of the rigid and flexible electrodes.

Features	**Conventional rigid electrode**	**New flexible polymer electrode**
Material	Si bulk	Polymer material (Parylene, PEDOT)
Mechanical stiffness	Hard	Flexible
Longitudinal stiffness	High	Low
Clutch mechanism	Cannot deform and fit to the opposite electrode → Large air gap	Deform and fit to the opposite electrode → Reducing the air gap
Voltages	High	Low

Table 3.2. Properties of different polymer films [39–43].

Characteristics	**Parylene**	**PI (polyimide)**	**Aramid**
Elastic modulus [GPa]	3.2	3	10
Permittivity [F/m]	2.3×10^{-11}	3.01×10^{-11}	3.27×10^{-11}
Tensile strength [MPa]	69	150	480
Density [g/cm^3]	1.29	1.42	1.44

drawbacks, the flexible electrode is designed with three layers that are composed of a conductive layer sandwiched between two insulating layers. This structure allows obtaining a thin bottom layer, and a desired thickness for the strength and flatness of the electrode.

Thermal treatment in the fabrication process produces the residual stress. This stress induces the bending of the flexible electrode. A conductive layer for the flexible electrode can be served as a metal thin film or a conductive polymer layer. The metal film can be fabricated using the vacuum deposition process while the conductive polymer layer can be formed by the spin-coating method. An insulating layer can be found in a conventional polymer film with a certain thickness that depends on the commercial production. Moreover, the insulating layer can be fabricated using the deposition method. The deposition and spin-coating methods allow controlling the thickness of the layer. But, these methods use thermal treatment in the process that causes the residual stress in the film, and therefore induces warping problem, especially with a thin metal film. We investigate characteristics of different materials that can be employed for the flexible electrode in following sections.

3.3.1. Insulating layer

In this section, we introduce several candidates for the insulating layer of the flexible electrode. The insulating layer should have thin thickness and high flexibility for better fit to the opposite electrode.

Table 3.3. Properties of different conductive polymers [29,44–47].

Characteristics	**PEDOT:PSS**	**Polyaniline**	**Polypyrrole**
Conductivity [S/cm]	200-600	0.001-10	0.001-100
Color	Colorless	Dark green	Urban
Features	- High transparency - High conductivity - Heat and light resistance	- Stable conductivity - Powder type - Wear resistance	- Conductivity without humidity dependence - Good stability over time

An insulating layer, which has flexible characterization, can be found in popular polymer materials in MEMS fields such as parylene, polyimide (PI), aramid, etc. (Table 3.2) [39–43]. The high flexibility of the polymer electrode can be achieved by low elastic modulus of the polymer materials. Further, it is important that the thickness of the electrode is controllable to obtain the desired thickness. A commercial aramid film (TORAY, Japan) has several thicknesses such as 12, 4.4, or 3.6 μm. A surface roughness (RMS) of the aramid film measured by atomic force microscopy (AFM) measurement was 12.152 nm. The warping phenomenon of this aramid film is small, but the film thickness is large and cannot be controlled. The 3.6 μm thick aramid film also has sticking problem with the contact electrode that causes a difficulty in relative sliding between them. A PI film is formed by a spin-coating method and a thermal treatment at high temperature (150 °C). This process causes thermal stress that reduces the flatness of the electrode. On the other hand, the thickness of a parylene film formed by vacuum deposition at temperature less than 50 °C can be controlled by the weight of the dimer. Hence, we employ the parylene film as an insulating layer of the flexible electrode in this study.

Figure 3.3. Image of the flexible electrode with an Au film on a parylene film substrate.

3.3.2. Conductive layer

A conductive layer serves as an electrode for the flexible electrode. As mentioned above, a metal thin film or a conductive polymer layer can be employed as an electrode. However, the residual stress inside a metal film causes a severe influence on the flatness (warping/ buckling) of the flexible electrode. Figure 3.3 shows the fabricated Au film with a thickness of 120 nm mounted on a 5 μm thick parylene layer using the evaporation method. We can observe a large warping problem of the Au thin film electrode in this situation. It indicates that a metal film is not an appropriate candidate for the flexible electrode.

A conductive polymer that combines the flexibility of organic compounds and the conductive inorganic conductors is expected to have applications in various fields such as solar cell, solid electrolytic capacitor, touch panel, etc. The characteristics of several conductive polymers are summarized in Table 3.3 [29,44–47]. Among these, poly (3, 4 - ethylenedioxythiophene) (PEDOT) has good electrical conductivity and transparency, higher flexibility and durability, and suffers from less cracking than metal electrodes. PEDOT also has a higher conductivity than other conductive polymers such as polyaniline and polypyrrole. In general, PEDOT is insoluble and it is dispersed in an aqueous solution with the presence of polystyrene sulfonic acid (PSS). Therefore, PEDOT:PSS thin film can be formed by heating to evaporate the solvent. In this study, PEDOT:PSS is spin-coated and baked at a low temperature (75 °C). Accordingly, the influence of the residual stress on this conductive layer is low for better flatness of the flexible electrode.

In this thesis, we consider and evaluate the flexible electrode that is composed of a conductive PEDOT layer sandwiched between insulating parylene layers, called a PEDOT−parylene electrode. The desired thickness of the electrode is controlled by the vacuum deposition process for the insulating parylene layer and the spin-coating process for the conductive PEDOT layer.

3.4. Fabrication method of flexible electrode

This section describes a method for fabricating the flexible PEDOT−parylene electrode. As mentioned in previous section, we use the deposition method to form insulating parylene layers and spin-coating method to fabricate the conductive PEDOT layer. The surface roughness of the bottom surface depends on the Si substrate owing to the fabrication method (step (1), Figure 3.4). Figure 3.4 shows the fabrication process of the PEDOT−parylene electrode. The fabricated condition is illustrated in Table 3.4. The flow steps corresponding with expression in Table 3.4 are described in detail blow:

(1) The bottom parylene layer of the electrode is deposited on the Si substrate.

(2-5) An Au layer as a protecting layer for the later RIE etching parylene process is deposited and patterned.

(6) The PEDOT layer is formed by a spin-coating process and then baked to evaporate the solvent.

(7) The top parylene layer is deposited to obtain desired thickness of the electrode.

(8-9) An AZ-4620 photoresist (Clariant Corporation, America) mask is patterned for the RIE etching parylene.

(10) The AZ-4620 photoresist mask is removed.

(11-13) The electrodes are separated by a laser cutting machine; electrical Cu wire is bonded to each electrode using conductive epoxy. Then, the electrodes are peeled off the substrate.

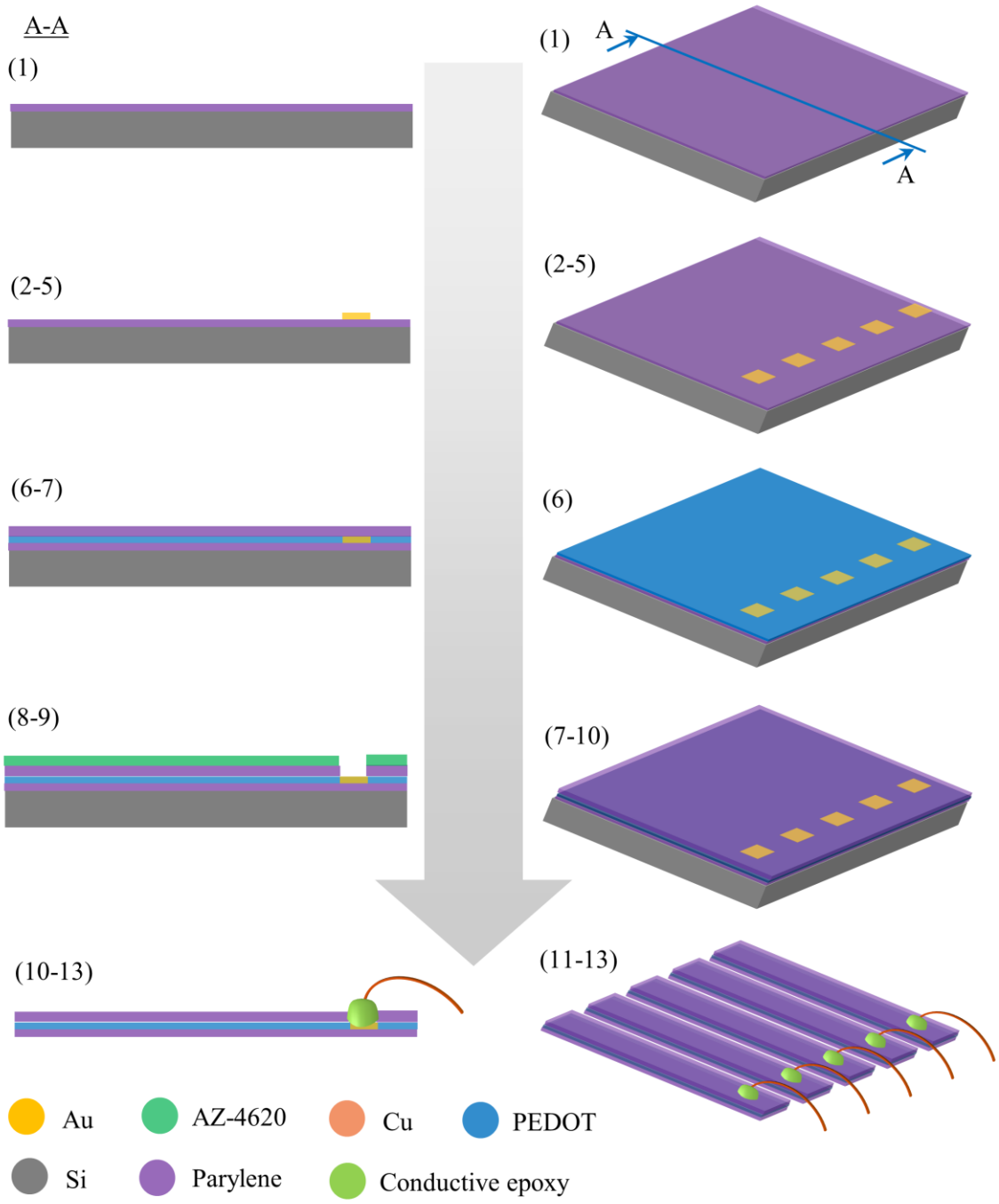

Figure 3.4. Schematic diagram of the fabrication process of PEDOT−parylene electrodes.

Table 3.4. Fabrication process conditions of the PEDOT−parylene electrode.

No	Process steps	Equipment/ process	Conditions	
1	Insulating layer deposition	Parylene deposition apparatus	Dimer	Parylene C
			Dimer amount	1.71 g
2	Au deposition	Vacuum evaporation system	Sample	Au
			Thickness	1200 Å
			Vacuum	1.0×10^{-5} Torr
			Current value	60 A
3, (8)	AZ mask for wet etching (for RIE etching parylene) Photolithography		Resist	AZ-4620 (54 cP)
		Spin coater	Spin coating	1st 500 rpm/10 sec
				2nd 3000 rpm/30 sec
		Hot plate	Pre-baking	110℃/90 sec
		Mikasa Exposure Machine	Exposure time	40 sec
			UV intensity	9.2 mJ/cm^2
		Developing solution (NMD-3)	Development	90 sec
		Hot plate	Post baking	110℃/5 min
4	Au etching		Etchant	Au etchant
			Time	About 1 min
5	Resist removal	Acetone	Time	5 min
6	PEDOT deposition		Thickness	160 nm
		Spin coater	Spin coating	1st 500 rpm/5 sec
				2nd 1500 rpm/35 sec
		Hot plate	Baking	75℃/20 min
7	Insulating layer deposition	Parylene deposition apparatus	Dimer	Parylene C
			Dimer amount	3.42 (6.84) g
9	RIE etching	RIE machine	Power	200 W
			Time	2 (4) min
10	Resist removal	Remover	Time	5 min
		Acetone	Time	5 min
11	Laser cutting	Excimer laser	Output	4.8 mJ
12	Wire bonding			Conductive epoxy
		Hot plate	Baking	80℃/5 min
13	Mechanical peel off			

Table 3.5. Characterization of the flexible electrodes in thickness.

Thin electrode	Thick electrode
+ Low applied voltages	− High applied voltages
− Difficult peel-off process	+ Easy peel-off process
− Difficult in forward motion due to low longitudinal stiffness	+ Easy movement
− High sticking force	+ Low sticking force

3.5. Fabrication results of flexible electrode

As discussed above, we expect a thin electrode for efficient electrostatic-force generation. However, a thinner electrode has higher sticking phenomenon, difficulty in peel-off process, and restriction in relative movement due to its lower longitudinal stiffness. The characterization of the flexible electrode is summarized in Table 3.5 in terms of thickness. The thickness is investigated to determine the optimal value. It is difficult to define the sticking phenomenon and geometric roughness of the Si surface that have effects on the peel-off process in fabrication of the electrode. We first fabricated a sample PEDOT−parylene electrode with an approximate thickness of 3 μm that consists of a 1 μm thick parylene bottom layer, a 160 nm thick PEDOT layer, and a 2 μm thick parylene top layer. The length and width of the electrode are 25 and 5 mm, respectively. The results show that the large warping nature of the fabricated electrode is affected by the mechanical peel-off process (Figure 3.5(*a*)). This result indicates that the thickness needs to be increased to improve the strength and flatness of the electrode. We then fabricated a thicker PEDOT−parylene electrode with approximate 5 μm thickness. This electrode has a 4 μm thickness of the parylene top layer, and the other sizes are similar with that of the 3 μm thick electrode. The result shows that the 5 μm thick PEDOT−parylene electrode has better flatness and lower warping (Figure 3.5(*b*)). We will investigate characteristics of this electrode in the following section.

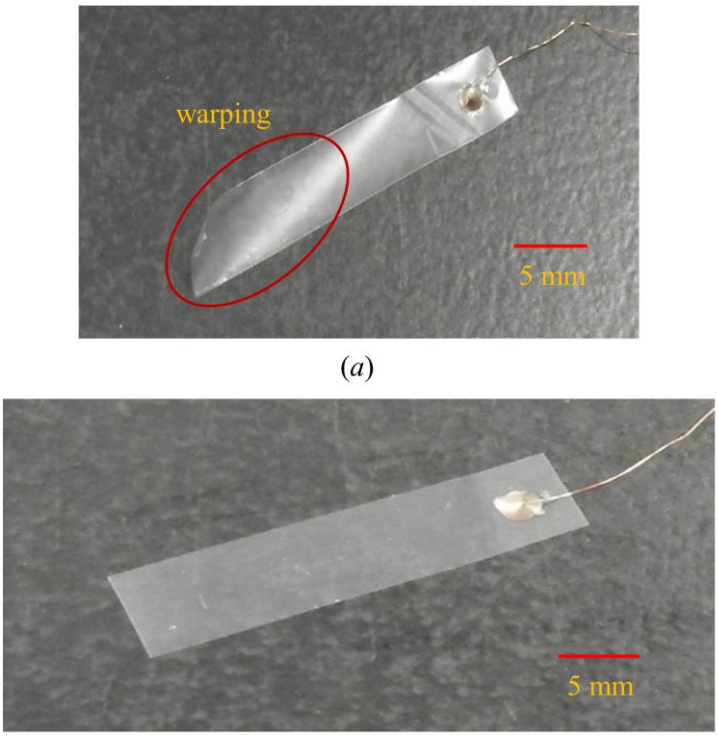

Figure 3.5. Images of PEDOT−parylene electrodes with the thickness of (*a*) 3 μm and (*b*) 5 μm.

3.6. Characteristics and application of flexible electrode

In this section, we evaluate the performance of the 5 μm thick PEDOT−parylene electrode. The important characteristics of the PEDOT−parylene electrode such as capacitance, air gap and electrostatic clutching force are investigated and compared to that of the Si bulk electrode.

3.6.1. Capacitance

As mentioned above, two opposite electrodes form the series capacitors with the dimensions of 25 mm length, 5 mm width, and insulating layers as a 1 μm thick parylene layer and an air gap. The parameters of the capacitors are summarized in Table 3.6. We evaluate the relationship between the capacitance and the air gap that crucially influence the efficiency of electrostatic-force generation in the ECLIA. If the insulating

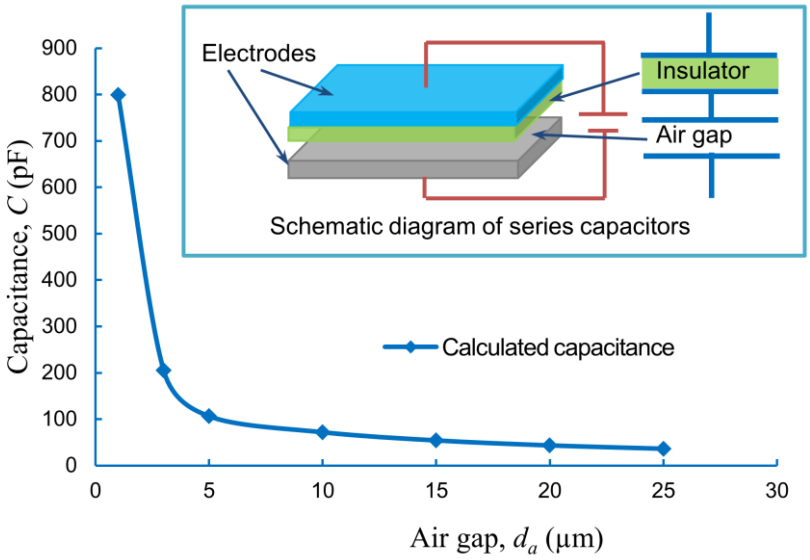

Figure 3.6. Calculated capacitance with respect to air gap.

layer and air gap are thinner, the capacitance is larger. Thus, the electrostatic force is higher when a voltage is applied to the opposite electrodes.

The equivalent capacitance is calculated using equation (2.1). From equation (2.2) we obtain the capacitances with insulating layers of parylene (C_i) and an air gap (C_a) as follows:

$$C_i = \frac{\varepsilon_i A}{d_i} \tag{3.1}$$

$$C_a = \frac{\varepsilon_a A}{d_a} \tag{3.2}$$

where $\varepsilon_{i,a}$ and $d_{i,a}$ are the permittivity and thickness of the insulating parylene layer (subscript *i*) and the air gap layer (subscript *a*), respectively; *A* is the overlap area of the opposite electrodes.

$$A = lb \tag{3.3}$$

Table 3.6. Parameters of the capacitors.

l **(m)**	***b*** **(m)**	d_i **(m)**	ε_i **(F m^{-1})**	ε_a **(F m^{-1})**
0.025	0.005	10^{-6}	2.3×10^{-11}	8.85×10^{-12}

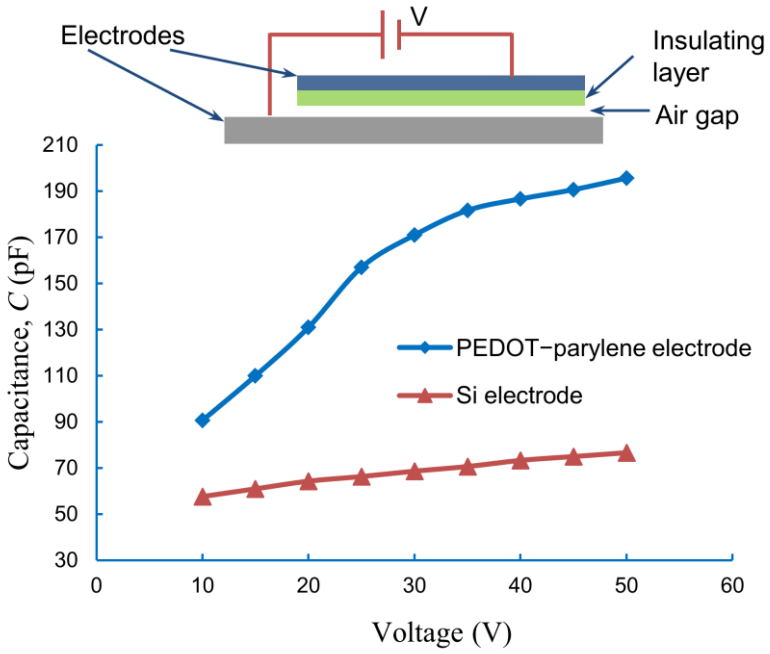

Figure 3.7. Measurement results of the capacitance between the PEDOT−parylene and Si electrodes (blue curve) and that between two Si electrodes (red curve).

where l and b are the length and width of the electrode, respectively.

Substituting (3.1), (3.2) and (3.3) into (2.1) we obtain

$$C(d_a) = \frac{\varepsilon_i \varepsilon_a lb}{\varepsilon_i d_a + \varepsilon_a d_i} \tag{3.4}$$

Substituting the determined values (see Table 3.6) into (3.4), we calculate the capacitance C with respect to the variable air gap d_a. Figure 3.6 shows the calculated capacitance versus the air gap. The results illustrate that the capacitance reduces remarkably when the undesired air gap increases from 0 to 5 μm. This indicates that the electrostatic-force generation improves significantly when the air gap is less than 5 μm.

The efficient electrostatic-force generation of electrodes can be evaluated by measuring the capacitance. We compared the capacitances between two Si bulk electrodes and that between the PEDOT−parylene and Si electrodes at the similar conditions. The capacitance was measured using a LCR meter (4284A, Agilent, Germany). Figure 3.7 shows the measured capacitances between two Si electrodes (the red curve) and those between the PEDOT−parylene and Si electrodes (the blue curve) at different applied voltages. The results show that the capacitance between the PEDOT−parylene and Si electrodes was much larger than that between two Si

electrodes due to the smaller air gap, resulting from the better fit to the contact electrode. The capacitance between two Si electrodes increased slightly from 58 pF to 77 pF (~ 33 %) when the applied voltages changed from 10 to 50 V, which corresponded to a 0.475 pF V^{-1}. This result indicates that the air gap decreased slightly due to hard contact surfaces of the Si electrodes. On the other hand, the capacitance between the flexible and Si electrodes increased remarkably from 91 to 157 pF (~ 73%) when the applied voltages changed from 10 to 25 V, corresponding to a 4.4 pF V^{-1}. When the applied voltages changed from 25 to 50 V, the capacitance increased slightly from 157 to 196 pF (~ 25%), corresponding to a 1.56 pF V^{-1}. It indicates the larger reduction in air gap at lower voltages of 25 V comparing with that at higher voltages of 25 V. The calculated value of the air gap is considered in the following section.

3.6.2. Air gap

It is difficult to measure an air gap between two contact electrodes. The air gap is inversely proportional to the capacitance (see equation (2.2)). In this section, we estimate the air gap d_a using the measured capacitance C mentioned in previous section. From the equivalent capacitance equation (2.1), we obtain

$$C_a = \frac{CC_i}{C_i - C} \tag{3.5}$$

Substituting (3.2) into (3.5) we obtain

$$d_a = \frac{\varepsilon_a A(C_i - C)}{CC_i} \tag{3.6}$$

Substituting the determined values (see Table 3.6) into (3.6), we calculate the estimated air gap d_a at various applied voltages V. Figure 3.8 shows the estimated air gap between two Si electrodes (the red curve), and that between the PEDOT−parylene and Si electrodes (the blue curve). The results indicate that the air gap between the PEDOT−parylene and Si electrodes was smaller than that between two Si electrodes due to the better fit to the contact electrode of the flexible electrode. The air gap between the flexible and Si electrodes was smaller than that between two Si electrodes approximately –37 % at the applied voltage of 10 V. However, the changing is approximately –59 % at 25 V. The air gap between two Si electrodes decreased slightly from 19 to 14 μm (~ –26 %) when the applied voltages increased from 10 to 50 V, which corresponded to a –0.125 μm V^{-1}. On the other hand, the air gap between the

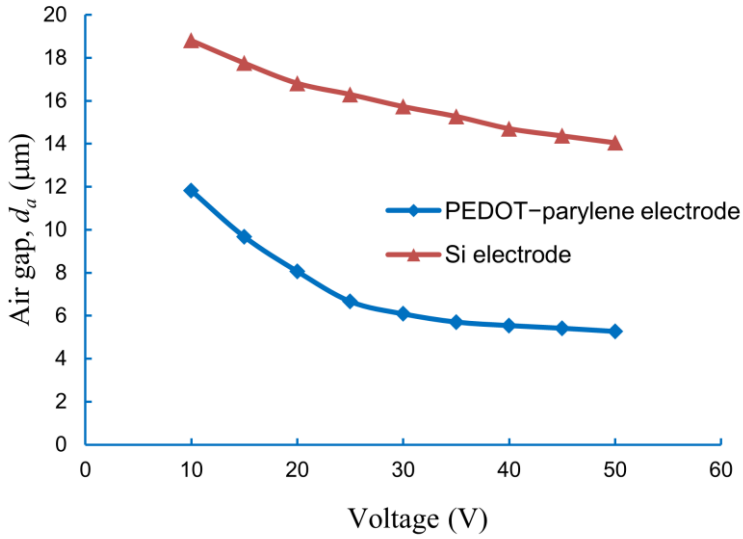

Figure 3.8. Air gap estimated from capacitance between the PEDOT−parylene and Si electrodes (blue curve), and that between two Si electrodes (red curve).

flexible and Si electrodes decreased remarkably from 12 to 6.7 μm (~ –44%) when the applied voltages increased from 10 to 25 V, corresponding to a –0.353 μm V^{-1}. When the applied voltages changed from 25 to 50 V, the air gap decreased slightly from 6.7 to 5.3 μm (~ –21%), corresponding to a –0.056 μm V^{-1}. It is indicated that the air gap decreased sharply owing to larger deformation of the flexible electrode when the applied voltages reached to 25 V. The air gap reduced slightly when the applied voltages were larger than 25 V because of the better fit at higher voltages. Therefore, the flexible electrode is expected to obtain efficient electrostatic-force generation to improve the performance of the electrostatic clutch mechanism at higher voltages of 25 V. The larger air gaps at lower voltages of 25 V results in lower efficiency of electrostatic-force generation.

3.6.3. Electrostatic clutching force

In this section, we investigate and compare the electrostatic clutching force between the PEDOT–parylene electrode and the Si one. The apparatus for measuring the electrostatic clutching force was shown in Figure 2.6.

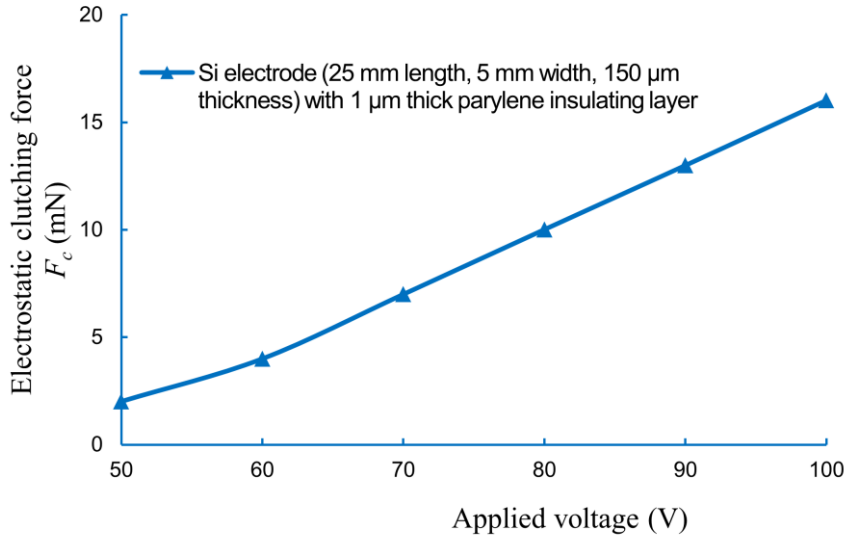

(*a*)

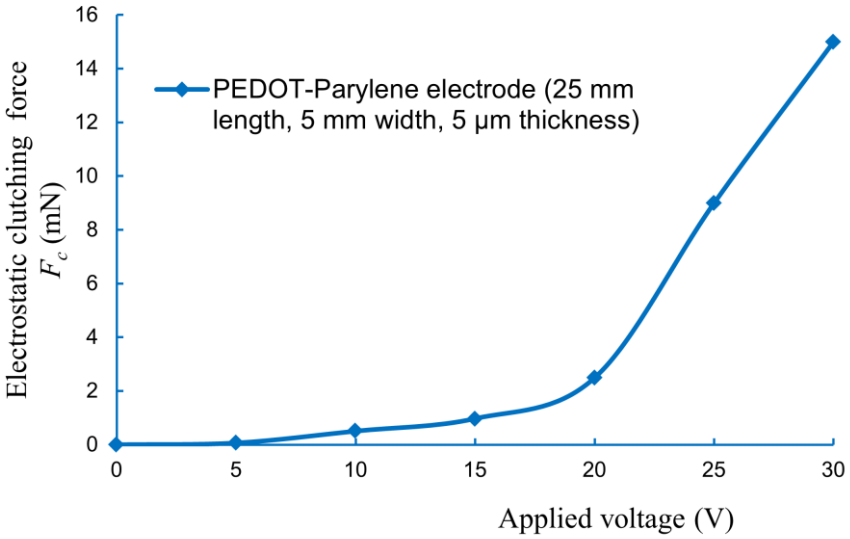

(*b*)

Figure 3.9. Measurement results of the electrostatic clutching force acting on (*a*) the Si electrode and (*b*) the PEDOT−parylene electrode.

As previously discussed, the air gap increases the distance between the contact Si electrodes, resulting in a reduction in the electrostatic force. Figure 3.9(*a*) shows the measurement of the electrostatic clutching force acting on the Si electrode. A clutching force of 16 mN is generated by the applied voltage of 100 V. The change in the clutching force in terms of the applied voltages is approximately 0.28 mN V^{-1}. The efficiency of electrostatic-force generation is rather low in this situation.

Figure 3.9(*b*) shows the measurements for the electrostatic clutching force acting on the PEDOT−parylene electrode. We found that this force increased slightly at voltages less than 20 V. When the applied voltage was larger than 20 V, the electrostatic clutching force increased rapidly, indicating that the air gap decreased sharply in this situation. The electrostatic clutching force acting on the flexible electrode at 30 V (15 mN) was nearly equal to that on the Si electrode at 100 V (see Figure 3.9(*a*)). It is indicated that the flexible PEDOT−parylene electrode with thinner insulating layer forms a smaller air gap, resulting in an improvement in the electrostatic clutching force compared to the Si electrode.

3.6.4. Flexible slider for ECLIA

The flexible electrode has been proposed for efficient electrostatic-force generation. This flexible electrode is employed as the flexible slider for the ECLIA. The flexible slider has low longitudinal stiffness, resulting in small pushing-force generation. This slider can be used for optical applications that do not require high pushing force. An improvement of the longitudinal stiffness will be considered to obtain higher pushing force in the next chapter.

3.7. Summary and discussion

In this chapter, we have explored the flexible PEDOT−parylene electrode that consists of a conductive PEDOT layer sandwiched between the parylene insulating films. This structure allows thinner bottom layer and desired thickness for better strength and less warping/ bending of the electrode. The flexible electrode could deform and fit to the contact electrode for decreasing the air gap and thus improving the electrostatic clutching force. The air gap, capacitance and electrostatic clutching force between the flexible and Si electrodes were evaluated and compared to those between two Si electrodes. The electrostatic clutching force acting on the flexible electrode at 30 V was nearly equal to that on the Si electrode at 100 V. The flexible electrode was employed as the flexible slider to obtain efficient electrostatic-force generation for the ECLIA. Nevertheless, the low longitudinal stiffness of the flexible slider results in small pushing-force generation. A fishbone structure will be introduced to improve the pushing force in the following chapter.

Chapter 4

FISHBONE SLIDER FOR HIGHER PUSHING-FORCE GENERATION

4.1. Overview

This chapter describes a method for improving longitudinal stiffness and flatness of the flexible slider in order to enhance the pushing force of ECLIAs. The pushing force is transmitted by the generated force from the PZT actuator incorporated with the electrostatic clutch mechanism. As mentioned in previous chapter, the flexible slider could deform and fit to the opposite electrode in order to reduce the air gap and to improve electrostatic clutching force. But, the flexible slider has low longitudinal stiffness, resulting in small buckling force. In this chapter, we propose a fishbone structure mounted on the flexible slider to have an improvement of the longitudinal stiffness. The fishbone structure only occupies a small area of the slider surface; therefore, the fishbone slider is expected to have a minor reduction in the flexibility by this structure for obtaining higher pushing-force generation. Design, fabrication, production result and characteristics of the proposed sliders are described in this chapter.

4.2. Design of fishbone structure

As mentioned above, the flexible slider can deform and fit to the contact electrode to achieve highly efficient electrostatic forces. However, the flexible slider has a low longitudinal stiffness (0.03 mN of buckling force) and thus generates a low pushing force. A pushing force is required for applications such as micro-syringe pumps [26]. The longitudinal stiffness needs to be increased to enhance the pushing force of the flexible slider. In this research, a single bone and a fishbone structure mounted on the flexible sliders have been introduced and investigated for this purpose. The experiments

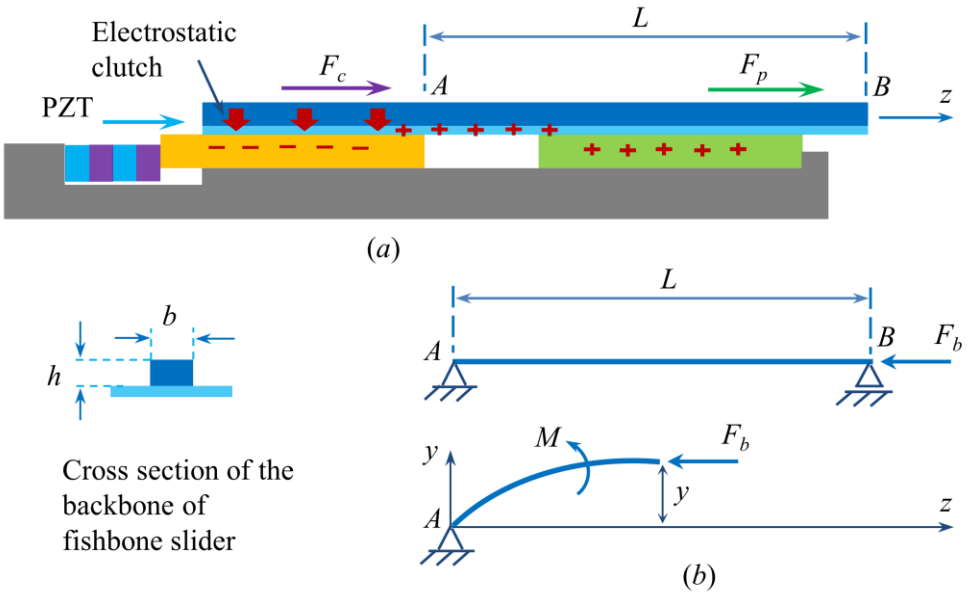

Figure 4.1. Diagram of (*a*) the force on the slider in the ECLIA and (*b*) the buckling-force calculation.

were carried out to evaluate characteristics of these sliders. The fishbone slider exhibited a better flatness than the single bone slider owing to the effect of perpendicular branches along the central ridge. The fishbone structure consists of a central ridge (backbone) with perpendicular branches (ribs) along it, as in Figure 4.2. The backbone improves the longitudinal stiffness and the ribs enhance the flatness of the slider. The flexibility of the slider is reduced by the fishbone structure, resulting in a decrease in the electrostatic clutching force. Nevertheless, the fishbone slider is expected to obtain higher pushing-force generation.

4.2.1. Backbone of fishbone structure

In this research, we first calculated the sizes of the backbone on the basis of the pushing-force requirement F_p. We then discussed and did experiments to find the optimal dimensions of the fishbone (backbone and ribs) structure.

Figure 4.1(*a*) shows the external force of the slider in the longitudinal direction, where F_p is the pushing force of the slider. The electrostatic clutching force F_c is calculated using equation (2.4). The frictional force F_f between the slider and the holding electrode can be neglected owing to its minor influence. The slider should not be buckled when applying the pushing force, meaning that the critical buckling force F_b

of the slider should be larger than the pushing force. Figure 4.1(*b*) shows a diagram of the buckling-force calculation. The buckling force yields a bending moment *M* and deflection *y*. From the schematic diagram, the moment balance equation is expressed as

$$\sum M = M + yF_b = 0 \tag{4.1}$$

$$M = -yF_b \tag{4.2}$$

Using the bending-moment equation for a small deflection, we obtain

$$y'' = \frac{M}{EI} = -\frac{F_b}{EI} y \tag{4.3}$$

$$y'' + \frac{F_b}{EI} y = 0 \tag{4.4}$$

where *E* is the elastic modulus, and *I* is the inertial moment of the backbone.

We define

$$k^2 = \frac{F_b}{EI} \tag{4.5}$$

Substituting the new expression in equation (7), we obtain

$$y'' + k^2 y = 0 \tag{4.6}$$

The solution to this equation is of the form

$$y = A\sin(kx) + B\cos(kx) \tag{4.7}$$

where *A* and *B* are found from the boundary conditions, which are

$$y(0) = 0 \rightarrow B = 0$$

$$y(L) = 0 = A\sin(kL) \rightarrow A = 0 \quad or \quad kL = n\pi \tag{4.8}$$

If $A = 0$, we have the seemingly trivial case where there is no deflection. The other solution is

$$k = \frac{n\pi}{L}, n = 1, 2, 3, ... \tag{4.9}$$

Substituting (4.9) into equation (4.5) we obtain

$$F_b = \left(\frac{n\pi}{L}\right)^2 EI \tag{4.10}$$

The slider will be buckled if the longitudinal force is larger than F_b. The critical load F_b increases as n increases; therefore, the lowest critical load is given by $n = 1$ as follows:

$$F_b = \left(\frac{\pi}{L}\right)^2 EI \tag{4.11}$$

The range of output force the MEMS actuator commonly exhibits is sub-mN [1–3]. The micro-actuators based electrostatic inchworm motion can produce an output force of ±0.11 mN [1] or ±0.45 mN [2]. In this research, we design the critical buckling force of the fishbone slider as 5 mN, corresponding to the maximum pushing force that the slider can generate. The longitudinal stiffness of the fishbone slider is approximately 166 times greater than that of the flexible slider (0.03 mN). The designed fishbone slider is expected to improve the pushing force compared to conventional MEMS actuators. The length of buckling part L is 7 mm, depending on our fabricated ECLIA. The cross-sectional area ($b \times h$) of the backbone was investigated on the basis of the residual stress that is influenced by different thermal coefficients. In the fabrication process of SU-8 3050, we determined that the thickness of the backbone h is 80 μm at a 1500 rpm spin-coating speed. The elastic modulus of SU-8 is 2×10^9 N m^{-2}. Finally, we obtain the width of the backbone from (4.11) as

$$b = \frac{12F_bL^2}{E\pi^2h^3} \tag{4.12}$$

Substituting the determined values into equation (4.12), we calculate b = 300 μm.

4.2.2. Ribs of fishbone structure

The fabrication process may cause the thin flexible slider to curve and bend, which is undesirable because the flatness of the flexible slider is lowered. If the slider stiffness is low, many ribs will be required to improve the slider flatness. However, it is difficult to exactly determine the slider flexibility. On the basis of these explanations, we carried out experiments to determine the rib length and the number of ribs.

4.3. Fabrication method of fishbone slider

This section describes a method for fabricating the fishbone slider that is composed of an SU-8 fishbone structure mounted on the flexible PEDOT−parylene slider. Figure 4.2 shows the fabrication process of the fishbone slider. The condition of the fabrication process is illustrated in Table 4.1. The flow steps corresponding with expression in Table 4.1 are described in detail below:

(1) The bottom parylene layer of the slider is deposited on the Si substrate.

(2-5) An Au electrode as a protecting layer for the later RIE etching parylene process is deposited and patterned.

(6) The PEDOT electrode layer is formed by a spin-coating process and then baked to evaporate the solvent.

(7) The top parylene layer is deposited to obtain desired thickness of the slider.

(8-9) An AZ-4620 photoresist mask is patterned for the RIE parylene process.

(10) The AZ-4620 photoresist mask is removed.

(11) The SU-8 3050 (MicroChem Corporation, America) photoresist is patterned for the fishbone structure.

(12-14) The sliders are separated by a laser cutting machine; electrical Cu wire is bonded to each slider using conductive epoxy. Then, the sliders are peeled off the substrate.

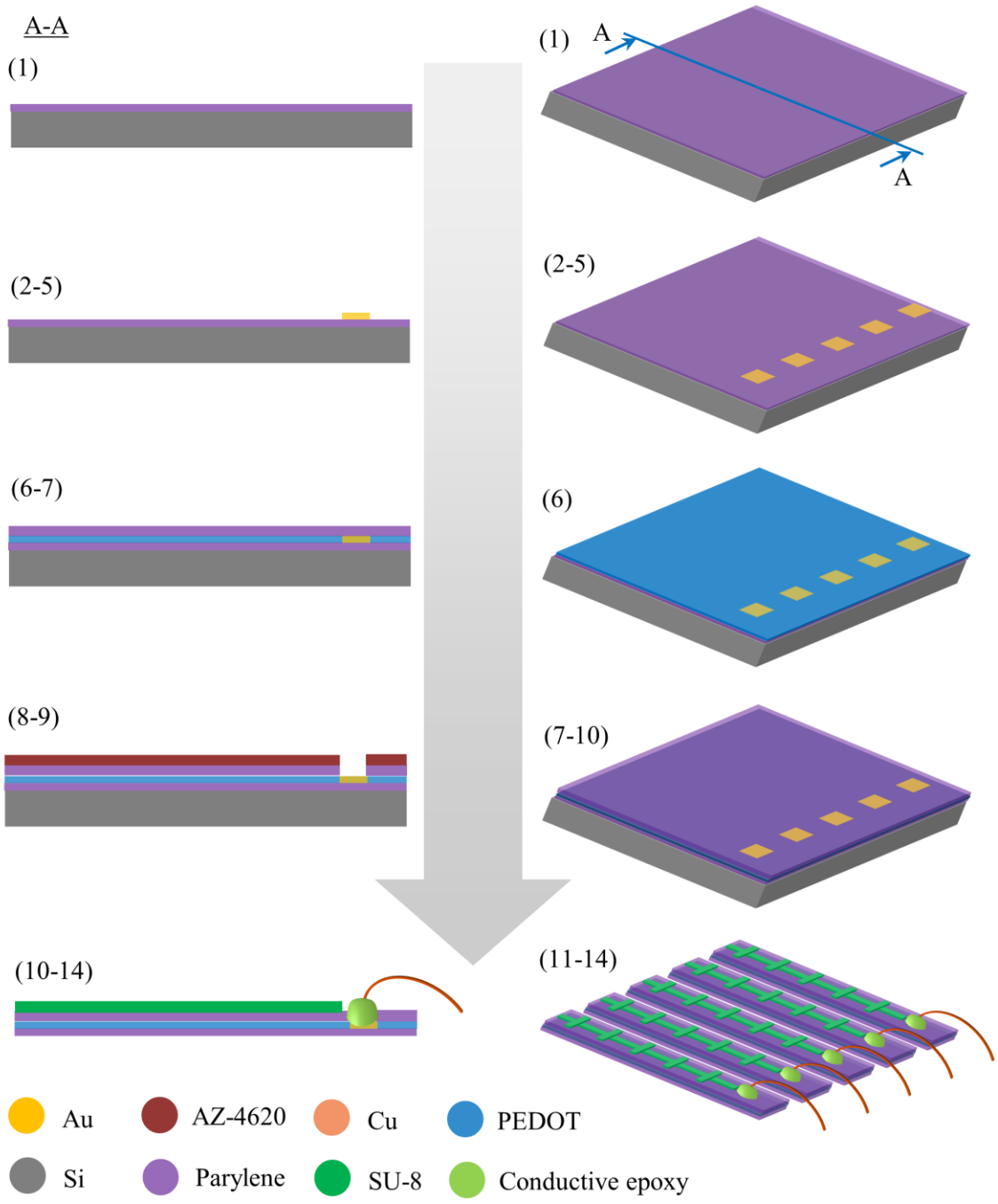

Figure 4.2. Schematic diagram of the fabrication process of the fishbone slider.

Table 4.1. Fabrication process conditions of the fishbone slider.

No	Process steps	Equipment/ process	Conditions	
1	Insulating layer deposition	Parylene deposition apparatus	Dimer	Parylene C
			Dimer amount	1.71 g
2	Au deposition	Vacuum evaporation system	Sample	Au
			Thickness	1200 Å
			Vacuum	1.0×10^{-5} Torr
			Current value	60 A
3, (8)	AZ mask for wet etching (for RIE etching parylene) Photolithography		Resist	AZ-4620 (54 cP)
		Spin coater	Spin coating	1st 500 rpm/10 sec
				2nd 3000 rpm/30 sec
		Hot plate	Pre-baking	110℃/90 sec
		Mikasa Exposure Machine	Exposure time	40 sec
			UV intensity	9.2 mJ/cm^2
		Developing solution (NMD-3)	Development	90 sec
		Hot plate	Post baking	110℃/5 min
4	Au etching		Etchant	Au etchant
			Time	About 1 min
5	Resist removal	Acetone	Time	5 min
6	PEDOT deposition		Thickness	160 nm
		Spin coater	Spin coating	1st 500 rpm/5 sec
				2nd 1500 rpm/35 sec
		Hot plate	Baking	75℃/20 min
7	Insulating layer deposition	Parylene deposition apparatus	Dimer	Parylene C
			Dimer amount	3.42 (6.84) g
9	RIE etching	RIE machine	Power	200 W
			Gas/ flow rate	O_2/30 sccm
			Pressure	0.05 Torr
			Time	2 (4) min
10	Resist removal	Remover	Time	5 min
		Acetone	Time	5 min

Table 4.1. Fabrication process conditions of the fishbone slider (continued).

No	Process steps	Equipment/ process	Conditions	
11	Fishbone structure SU-8 Photolithography		Resist	SU-8 3050
		Spin coater	Spin coating	1st slope/10 sec
				2nd 1000 rpm/10 sec
				3rd slope/10 sec
				4th 2000 rpm/70 sec
		Hot plate	Pre-baking	65℃/5 min; 95℃/15 min
		Mikasa Exposure Machine	Exposure time	35 sec
		Hot plate	Post baking	95℃/15 min
		Developing solution (SU-8 Developer)	Development	5 min
		Hot plate	Hard baking	95℃/1 min
12	Laser cutting	Excimer laser	Output	4.8 mJ
13	Wire bonding			Conductive epoxy
		Hot plate	Baking	80℃/5 min
14	Mechanical peel off			

4.4. Fabrication result of fishbone slider

In this research, the SU-8 fishbone structure mounted on the PEDOT−parylene slider (25 mm length, 5 mm width, and 5 μm thickness) was designed. The dimensions of the fishbone structure are b = 300 μm and h = 80 μm; the rib length and the distance between two adjacent ribs are 3 mm and 4.5 mm, respectively. Figure 4.3 shows an image of the fabricated slider. We will investigate characteristics of this slider in the following section.

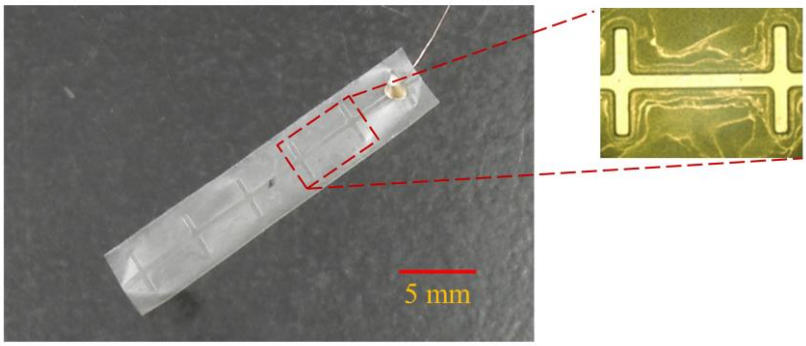

Figure 4.3. Image of the fishbone slider.

4.5. Characteristics of fishbone slider

In this section, we evaluate the performance of the fabricated fishbone slider. The capacitance, air gap and electrostatic clutching force between the fishbone slider and the Si electrode are investigated and compared to that between the PEDOT−parylene slider and the Si electrode. The pushing force of the fishbone slider is compared with that of the Si slider.

4.5.1. Capacitance and air gap

As mentioned above, the fishbone structure reduces the flexibility and increases the bending/wrapping of the slider. These characteristics can be evaluated by measuring the capacitance. We compare the capacitances of the flexible slider with and without the fishbone structure at similar conditions. Figure 4.4(*a*) shows the measured capacitance between the fishbone slider and the Si electrode (the purple curve), and that between the PEDOT−parylene slider and the Si electrode (the blue curve) at different applied voltages. The result shows that the capacitance between the PEDOT−parylene slider and the Si electrode was slightly larger than that between the fishbone slider and the Si electrode. It indicates that the air gap between the fishbone slider and the Si electrode was slightly larger than that between the PEDOT−parylene slider and the Si electrode due to the fishbone structure (see Figure 4.4(*b*)). In other words, the fishbone structure had minor influence to the slider bending.

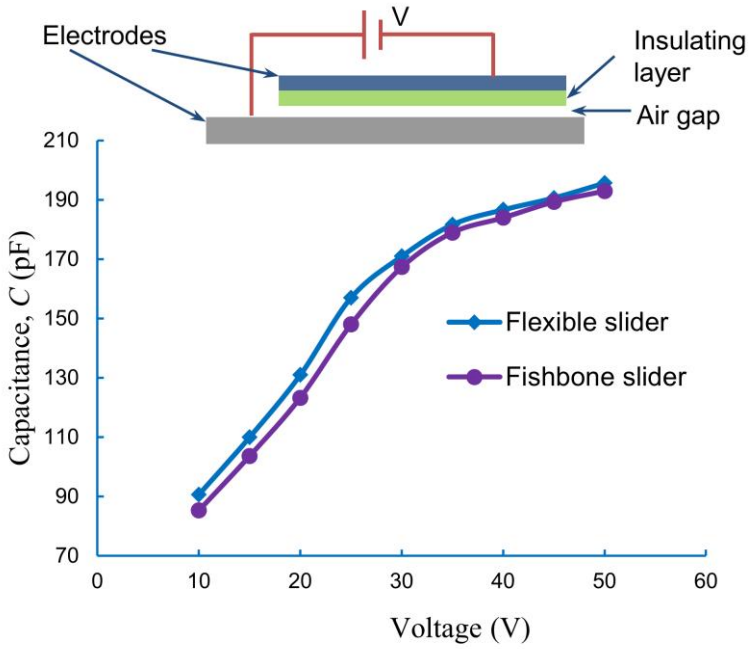

(*a*)

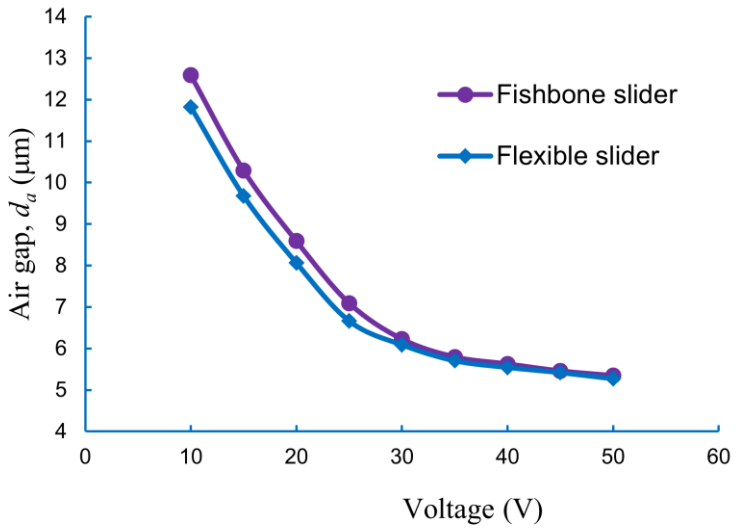

(*b*)

Figure 4.4. (*a*) Measured capacitance and (*b*) estimated air gap at different voltages.

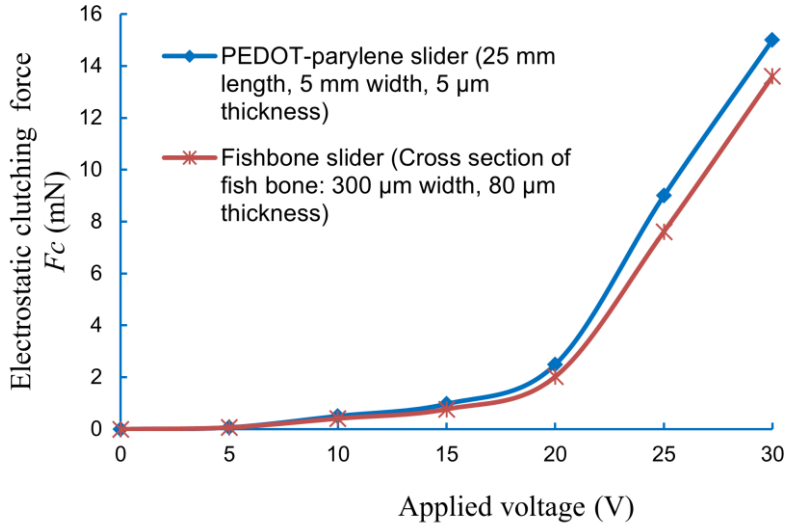

Figure 4.5. Measurement results of the electrostatic clutching force acting on the fishbone slider (red curve) and the PEDOT−parylene slider (blue curve).

4.5.2. Electrostatic clutching force

This section describes the properties of the electrostatic clutching force acting on the fishbone slider. As discussed in previous section, the fishbone structure causes an increase in the air gap. This phenomenon will decrease the generated electrostatic force. The electrostatic clutching force acting on the fishbone slider was measured to evaluate the performance in electrostatic-force generation (the red curve in Figure 4.5). The results show that the measured force acting on the fishbone slider was smaller than that on the flexible slider (the blue curve in Figure 4.5) by approximately 10% at an applied voltage of 30 V. This indicates that the fishbone structure reduced the flexibility of the fishbone slider. Nevertheless, it was expected to improve the pushing force.

4.5.3. Pushing force

In this section, the pushing force of the fishbone slider was investigated and compared with that of a Si slider. If the applied voltage increases, the electrostatic-clutching force increases, resulting in the better clutch mechanism. The electrostatic clutch mechanism also depends on the driving frequency of the voltage signal. If the driving frequency is

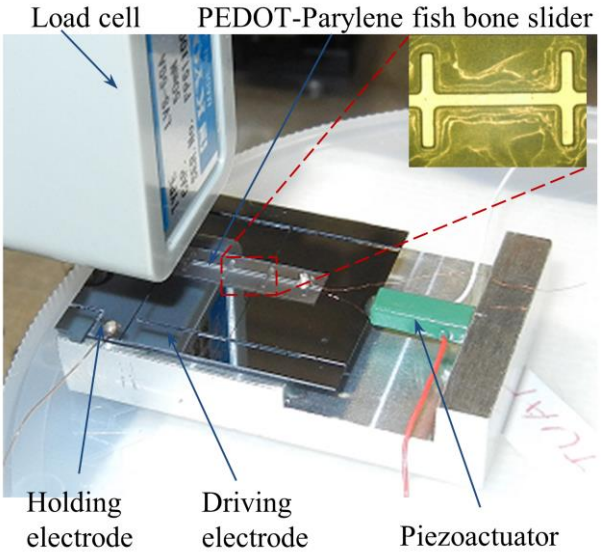

Figure 4.6. Photograph of the experimental measurement of the pushing force generated by the fishbone slider.

smaller, the clutch mechanism is less relative sliding. The pushing force will be measured at different conditions to evaluate the performance of the slider.

Figure 4.6 shows a photograph of the apparatus for measuring the pushing force of the fishbone slider. Figure 4.7 shows the pushing forces of the Si and fishbone sliders with respect to frequency. Various voltages (20, 30, and 50 V) were supplied to the PZT actuator; 100 and 70 V were applied to the electrostatic clutch mechanism for the Si and fishbone sliders. A higher frequency generated a lower pushing force. This characterization indicated that the electrostatic clutch mechanism at a higher frequency was less stable than that at a lower frequency. The pushing forces of the fishbone sliders were larger than those of the Si sliders even at lower applied voltages. Therefore, the fishbone slider considerably improves the pushing force. A decrease in the frequency and an increase in the applied voltage result in an improvement in the pushing force.

The pushing force of the fishbone slider was also considered with respect to the displacement at lower applied voltage (20 V) and higher frequency (20 Hz) that were the severe conditions of pushing force mentioned above (the blue curve in Figure 4.8). We also consider the pushing force at the higher voltage of 50 V and the similar frequency of 20 Hz (the red curve in Figure 4.8). Figure 4.8 shows that the pushing force decreased when the displacement of the slider increased. The pushing force at a higher voltage was larger than that at a lower voltage. These results indicated that the pushing force depended on the length of the cantilever, defined by the distance from the

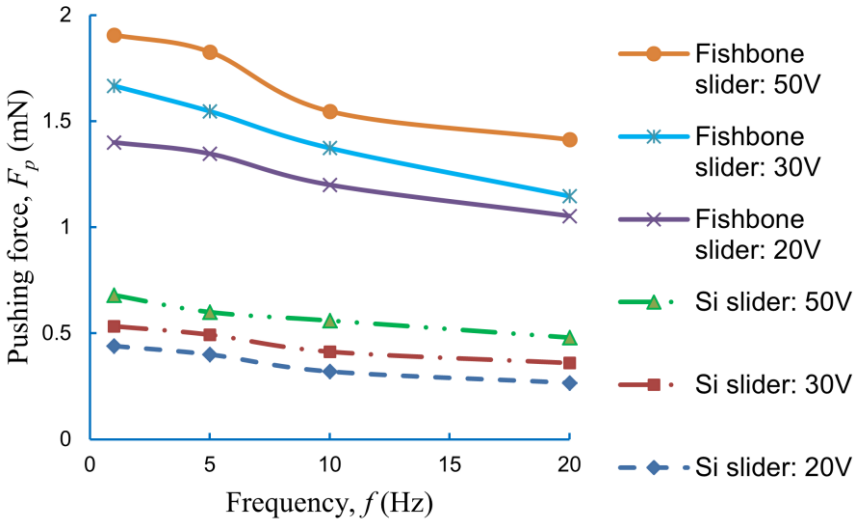

Figure 4.7. Measurement results of the pushing forces generated by the fishbone and Si slider.

last contact point with the driving electrode to the tip of the slider. A longer cantilever had a lower stiffness, resulting in lower pushing-force generation of the slider.

4.6. Summary and discussion

We have explored the fishbone slider consisting of the SU-8 fishbone structure mounted on the PEDOT–parylene slider for an improvement in pushing-force generation of the ECLIA. The buckling force of the fishbone slider is 5 mN that is 166 times larger than that of the flexible slider (0.03 mN). The pushing force of the fishbone slider gives greater improvement with three and four times larger than the Si slider and the inchworm actuator [2], respectively. This pushing force is sufficient for most applications of the ECLIA. We can conclude that the fishbone slider exhibited a significant improvement in pushing-force generation for further applications of the ECLIA.

In future work, a probe dipped in μpool (PDP) connection [31] will be utilized to eliminate a mechanical restriction of the electrical wiring connection for the slider. This improvement will further enhance the efficiency in pushing-force generation for the ECLIA. In the next chapter, the PDP connection technology and micro-potentiometer are applied for position feedback control of the ECLIA.

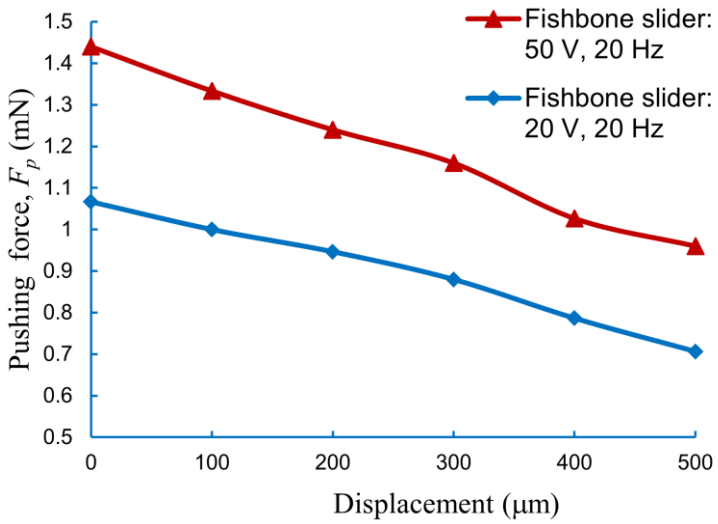

Figure 4.8. Measurement results of the pushing forces generated by the fishbone slider versus the displacement.

Chapter 5

POSITION FEEDBACK CONTROL FOR ELECTROSTATICALLY CONTROLLED LINEAR ACTUATOR

5.1. Overview

In this chapter, a position feedback controller using a micro-potentiometer and microcontroller is introduced to obtain higher performance for the ECLIA. The tuning parameters are investigated to choose their optimal values for adjusting the driving signal for the ECLIA. A micro-potentiometer mounted on the slider is utilized to detect the displacement without mechanical restriction of the slider. This is an important factor for feedback control of the ECLIA. The real position detected using the micro-potentiometer is converted to a digital value by an analog-to-digital converter (ADC) module inside the microcontroller. The microcontroller program calculates the error, which is defined as the difference between the reference and feedback values, to generate a suitable control signal to the ECLIA. The feedback control system is expected to reduce control time, overshoot, and steady-state error. The design, implementation and results of the feedback controller are presented in this chapter.

5.2. Design and implementation of ECLIA feedback control

5.2.1. Proportional-integral (PI) controller

The slider was operated by the stepwise motion; a fine stepping displacement of the slider in the order of nanometers is obtained by the PZT actuator that is driven by the applied voltage. The velocity of the slider is proportional to frequency of the driving voltage. Hence, we design a feedback controller that controls frequency of the voltage supplied for the ECLIA. This control method aims to reduce control time and a fine-precision approach to the desired position.

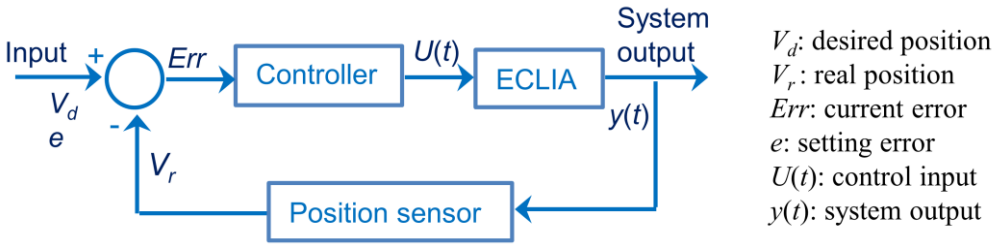

Figure 5.1. Block diagram of the ECLIA feedback control system.

Figure 5.1 shows a block diagram of the feedback control system. In this configuration, the controller block computes and generates the control signal to the system (ECLIA). The position sensor detects the real position of the slider V_r. The current error *Err* is the difference between the real value V_r and desired value V_d. This error signal is utilized by the controller to adjust the control input $U(t)$ to allow the system output $y(t)$ to reach the desired position. This configuration has advantages such as diminishing the effects of disturbance inputs, improving the response time of the system output, and compensating the steady-state error.

A PID controller is employed for feedback control. The proportional term adjusts a change of the system output that is proportional to the current error value. The integral term added to the proportional term accelerates the movement of the process toward the desired point. The derivative term slows the rate of change of the controller output to reduce the magnitude of the overshoot. Among the three terms, the derivative term is sensitive to measured noise, which can prompt an oscillation and instability of the system. Control parameters are utilized to adjust control input for the system. For tuning the control parameters, the control system can be performed as a mathematical model, and the control parameters are evaluated and chosen on the basis of the dynamic model. Otherwise, the real system is investigated to select the optimal values of control parameters. We use the ECLIA system to directly investigate the control parameters for this application.

In this study, the proportional term moves the slider to the set point with a velocity that is proportional to the current error value. The integral term accelerates the movement of the slider to the desired position by generating higher driving frequency. The vibration of the slider caused by the stepping motion and electrostatic clutch mechanism brings disturbance inputs or noise to the position sensor. The differentiation of an error signal amplifies noise. Thus, the noise affects to the derivative term and prompts instability of the system. The derivative term is removed from the controller.

Table 5.1. Characteristics of an AT90S8535 microcontroller.

Features	**AT90S8535**
Programmable I/O Lines	32
Data converter (ADC)	8 channels, 10 bits
Programmable Flash (bytes)	8K

We utilize a PI controller for the feedback control of the ECLIA system. The PI controller output is

$$u(t) = K_p Err(t) + K_i \int Err(t)dt \tag{5.1}$$

where K_p and K_i are the proportional and integral gains, respectively.

The standard form of the PI controller is discretized for implementing with a microcontroller. We design an algorithm for the ECLIA system. At the step k^{th} of the slider, the error value *Err(t)* is expressed as $Err(t_k)$. The integral term is calculated using

$$\int Err(t)dt = \sum_{j=1}^{k} Err(t_j) \tag{5.2}$$

Substituting the new expression into (5.1), we obtained the discrete PI controller $u(t_k)$ as follows:

$$u(t_k) = K_p Err(t_k) + K_i \sum_{j=1}^{k} Err(t_j) \tag{5.3}$$

As discussed previously, the stepwise motion of the slider is transmitted from the motion of the PZT actuator combined with the clutch mechanism. We can use the applied voltage to the PZT actuator for position control of the ECLIA. The higher applied voltage to the PZT generates its larger motion for producing the larger stepwise motion. The lower voltage is supplied to the PZT for the smaller stepwise motion and thus better position control when the slider approaches to the desired position. However, the higher voltage consumes higher power and might cause the damage of the microcontroller circuit. The control system without tuning gains produces the constant stepwise motion with larger value at higher voltages. Otherwise, the feedback control using tuning gains allows reducing the applied voltage to generate the reduction in

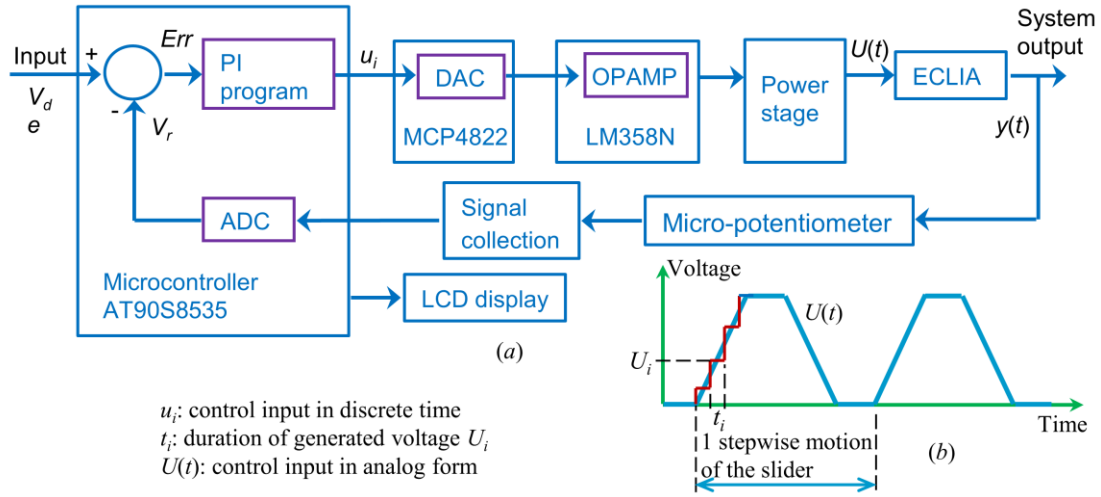

Figure 5.2. Feedback control of the ECLIA system: (*a*) block diagram of the control scheme and (*b*) an analog signal for the PZT actuator.

stepwise motions. Multiple stepwise motions obtain the large motion of the slider. This research also focuses on high-efficient electrostatic-force generation using the flexible electrode as stated in chapter 3. We can reduce the voltage to avoid the above mentioned drawback. We consider another solution using frequency control. This control method utilizes a feedback signal to compute a driving voltage with a gradual reduction of frequency by time. As the larger error signal, the higher driving frequency is generated to decrease the control time. When the error is smaller, the lower driving frequency is produced for obtaining stable motion and a fine-precision approach to the desired position. This control method aims to reduce control time, overshoot, and oscillation.

The tuning gains are important factors that affect the control signal. The larger tuning gains produce the higher driving frequency for reducing the response time. Nevertheless, it might cause overshoot and oscillation. We adjust these tuning gains to optimize the system output for the ECLIA with shorter response time, no overshoot, no oscillation. The tuning parameters depend on stepwise motion of the slider because of the instability of the clutch mechanism, and uncertainty of the slider movement. The larger stepwise motion of the slider intends to the shorter response time, and allows choosing the smaller tuning gains. The simple control system is first mentioned with only proportional gain to investigate the system output. If overshoot occurs, the integral gain will be adjusted while reducing the magnitude of the proportional gain to improve the control quality.

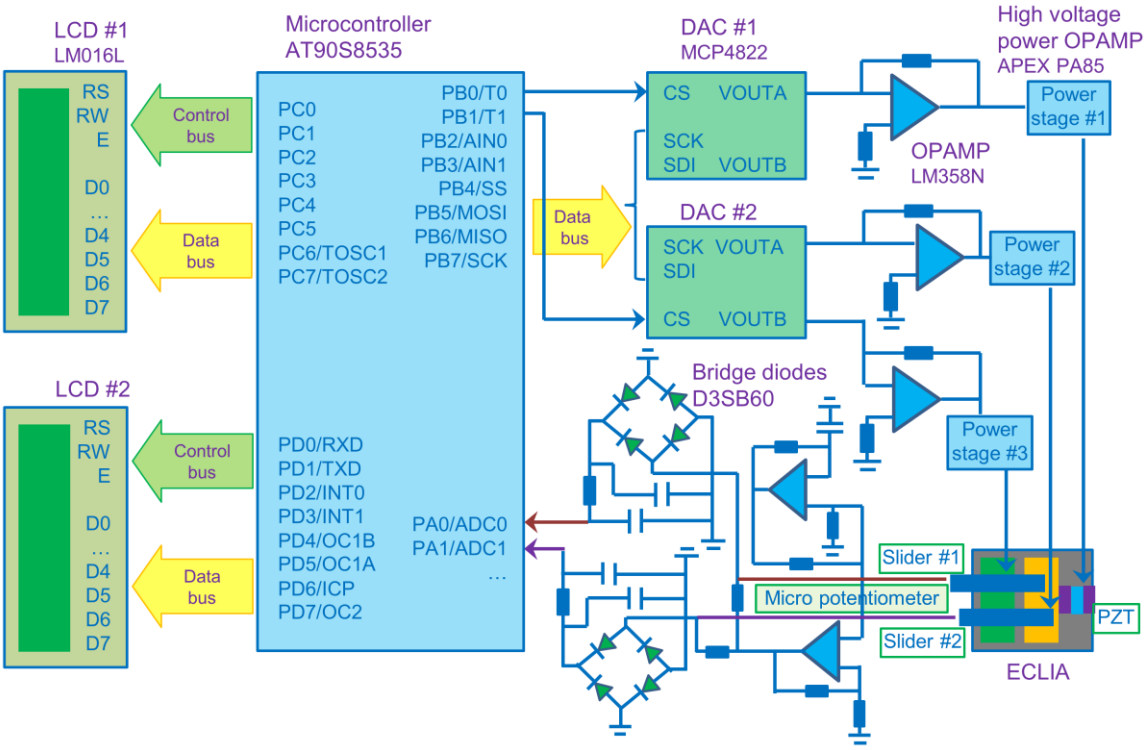

Figure 5.3. Schematic diagram of the ECLIA control system.

5.2.2. Electrical circuit for microcontroller

In this section, we design an electrical circuit that computes and generates control signals for the ECLIA. A control unit is one of the most important parts of the electrical circuit. We can find various candidates of control devices such as a microcontroller and a programmable logic controller (PLC). Among these, a microcontroller is simple, compact and mobile [48,49]. It can also be used with various programming languages and control methods. Taking these considerations into account, we designed a numerical feedback control system using an AT90S8535 microcontroller with the specifications listed in Table 5.1. The 32-port programmable I/O is sufficient for common peripheral devices such as analog-to-digital converter (ADC) inputs, and digital-to-analog converter (DAC) and LCD display outputs. This microcontroller has a 10-bit ADC module that can convert analog signals from the position sensors. Its 8-KB programmable flash memory meets the capacity requirement of the control program. Figure 5.2(*a*) shows a block diagram of the control scheme, which comprises the AT90S8535 microcontroller, a 12-bit DAC module MCP4822, an operational amplifier (OPAMP) LM358N, a power stage, and the ECLIA. The feedback branch consists of a

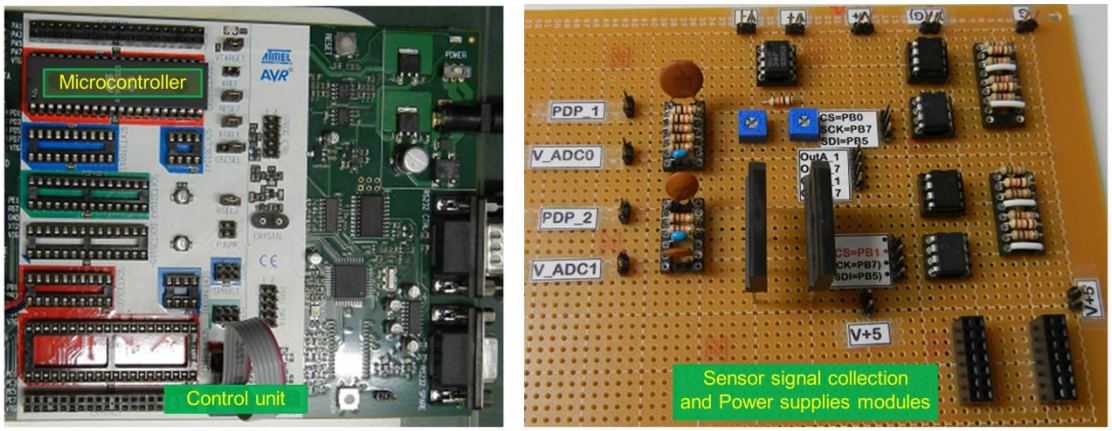

Figure 5.4. Images of the electrical circuit of the ECLIA control system.

micro-potentiometer and signal-collection module. This design incorporates LCD monitors to display the actual and desired positions of the sliders in digital values.

The current position of the slider is detected using a micro-potentiometer. The received signal is converted to a digital value V_r by the ADC module. The microcontroller program computes the current error *Err* and then compares it to the setting error *e*. If the current error is larger than the setting error, a digital signal will be generated and converted to an analog signal by a DAC module. The analog signal is then amplified by a power stage to supply to the ECLIA for one stepping motion of the slider. This loop is repeated as many times as necessary until the actual error is less than or equal to the setting error. This indicates that the slider has already reached the desired position. Figure 5.2(*b*) shows a wave form of an analog signal $U(t)$ supplied to the PZT actuator. The motion of the PZT actuator from periodic pulse *T* yields a stepwise motion of the slider. At the step k^{th} of the slider, the digital voltage u_i corresponding to the analog voltage U_i at the rising edge (Figure 5.2(*b*)) is calculated using

$$u_i = iu(t_k), i = 0,1,...,n \tag{5.4}$$

The maximal value of the digital voltage u_i is 4096 (12-bit DAC module MCP 4822). Consequently, the number of steps *n* for the rising edge is

$$n = \frac{4096}{u(t_k)} \tag{5.5}$$

As the larger error signal *Err*, the PI controller output $u(t_k)$ is larger (see Eq. (5.3)) and therefore the number of steps *n* is smaller. The control program requires shorter

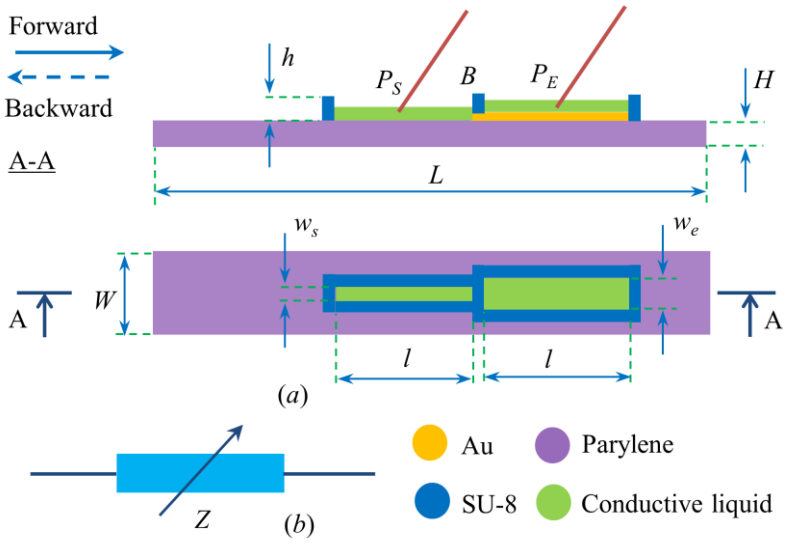

Figure 5.5. Micro-potentiometer using a PDP connection: (*a*) schematic diagram and (*b*) modeling.

time to compute the output signal, and the higher driving frequency will be produced. In contrast, the lower driving frequency will be generated.

Figure 5.3 shows a schematic diagram of the ECLIA control system. In this design, two sliders are introduced, and their positions are displayed on two LCD modules. Figure 5.4 shows images of the electrical circuit boards for the ECLIA control system. The board on the left is the control unit containing the AT90S8535 microcontroller, whereas the board on the right holds the power supplies and sensor signal collection modules. Together these boards provide the output stage to control the ECLIA. The accuracy of the position control depends on the number of bits used in the ADC module (10 bits). Each binary number from the ADC represents a certain voltage level (certain slider position). Hence, the accuracy is defined by the smallest input voltage (the smallest detected distance) that a digitizer can capture. The accuracy of the position control is 4.88 mV (5000 mV / 1024), which corresponds to one increment of the digital value under this condition.

5.2.3. Position sensor

A sensor for detecting the position of the slider is one of the most important parts in the feedback control of the ECLIA system. The sensor should have a high resolution and small physical restriction to the slider. A laser displacement meter using the triangle measurement principle (Micro-epsilon ILD 2200-2LL) can detect the movement of an object with nanometer resolution. Nevertheless, it requires a reflective surface and a

large space to set up the measurement system. It is difficult to detect the position of multiple sliders. A compact micro-potentiometer using a PDP connection with low physical restriction and a resolution in micro-meter range has been developed to detect the position of the slider [31]. We utilize the micro-potentiometer for the position feedback control.

The micro-potentiometer mounted on the slider (Figure 5.5(*a*)) comprises two probes dipped in two μpools. The first μpool having a thin Au bottom layer (120 nm in thickness) is called the electrode μpool. The other one is called the sensing μpool. The Au bottom layer of the electrode μpool connects to the sensing μpool at the end electrode *B*. The length *l*; widths w_e and w_s; and height *h* of the μpools are shown in Figure 5.5(*a*). A conductive liquid (1-ethyl-3-methyl, conductivity: 10 mS cm^{-1}) is injected into the two μpools to form an electrical–liquid connection and an ionic liquid resistor. Two probes are dipped into two μpools at P_E and P_S, resulting in non-mechanical connections. The relative position of the probes and the slider can be determined by the relative resistance of the ionic liquid measured between the two probes. The micro-potentiometer can be modeled as a variable resistor shown in Figure 5.5(*b*). If the slider moves forward or backward, the relative resistance *Z* between the two probes will change in direct proportion to the slider displacement. Consequently, the micro-potentiometer can be utilized to detect the position without interfering motion of the slider.

We also designed a μpool and probe as a PDP connection to supply an electrical signal to the slider. Figure 5.6(*a*) shows the fabrication process of the micro-potentiometer mounted on the flexible PEDOT–parylene slider. The condition of the fabrication process is illustrated in Table 5.2. The flow steps corresponding with expression in Table 5.2 are described in detail below:

(1) The bottom parylene layer of the slider is deposited on the Si substrate.

(2-5) An Au electrode is deposited and patterned.

(6) The PEDOT electrode layer is formed by a spin-coating process and then baked to evaporate the solvent.

(7) The top parylene layer is deposited to obtain desired thickness of the slider.

(8-12) An Au layer is deposited and patterned for the RIE parylene process.

(13-15) An Au electrode of the micro-potentiometer is patterned.

(16) The SU-8 3050 photoresist is patterned for the μpools.

(17-19) Sliders are separated by a laser cutting machine; conductive liquid is filled into the μpools. Then, the sliders are peeled off the substrate.

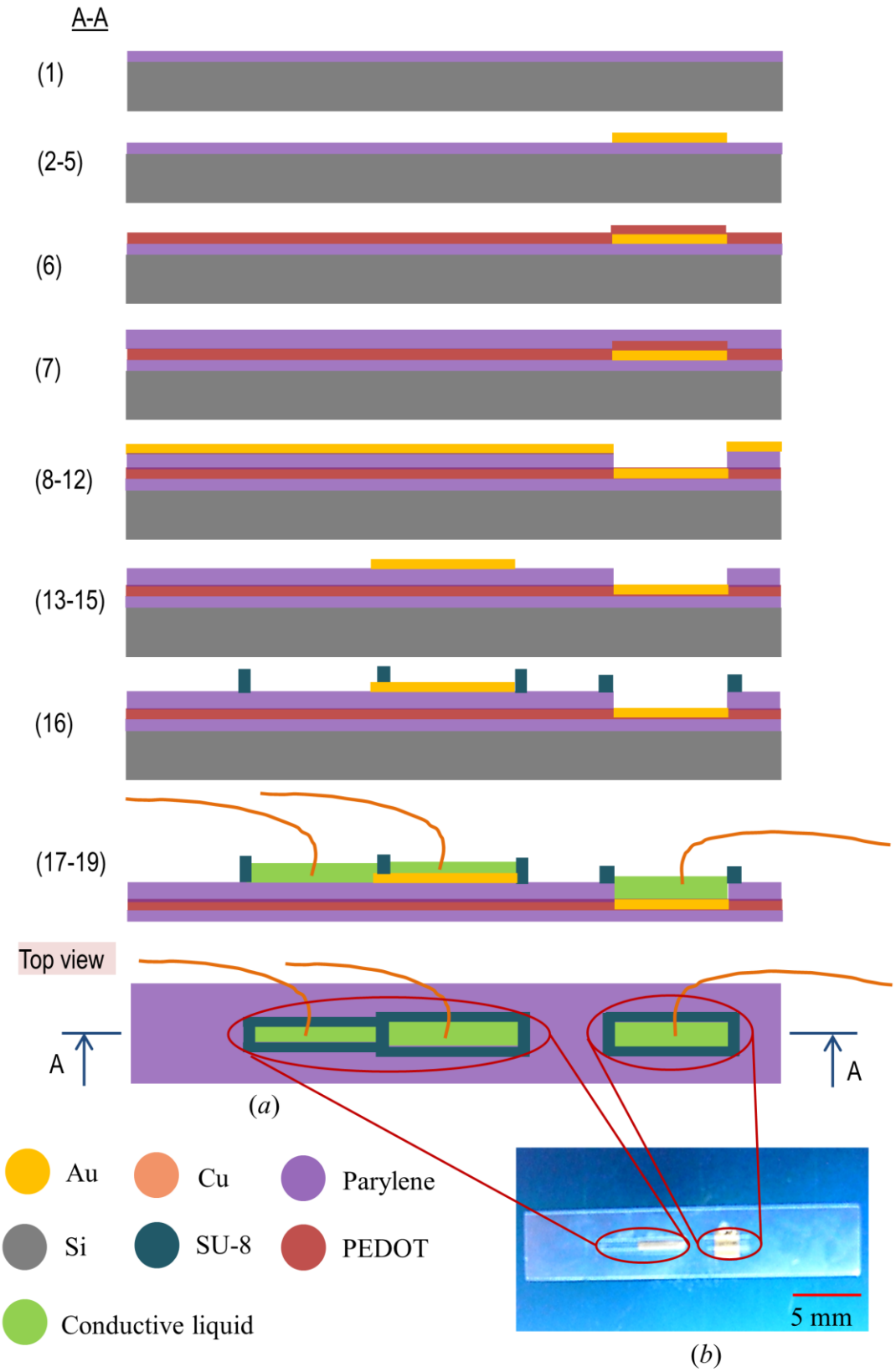

Figure 5.6. The micro-potentiometer using a PDP connection mounted on the PEDOT–parylene slider: (*a*) schematic of the fabrication process in cross-sectional A-A and (*b*) an image of the fabricated slider.

Table 5.2. Fabrication process conditions of the micro-potentiometer mounted on the flexible slider.

No	Process steps	Equipment/ process	Conditions	
1	Insulating layer deposition	Parylene deposition apparatus	Dimer	Parylene C
			Dimer amount	1.71 g
2, 8	Au deposition	Vacuum evaporation system	Sample	Au
			Thickness	1200 Å
			Vacuum	1.0×10^{-5} Torr
			Current value	60 A
3, 9, 13	AZ mask for wet etching (Photolithography)		Resist	AZ-4620 (54 cP)
		Spin coater	Spin coating	1st 500 rpm/10 sec
				2nd 3000 rpm/30 sec
		Hot plate	Pre-baking	110℃/90 sec
		Mikasa Exposure Machine	Exposure time	40 sec
			UV intensity	9.2 mJ/cm^2
		Developing solution (NMD-3)	Development	90 sec
		Hot plate	Post baking	110℃/5 min
4, 10, 14	Au etching		Etchant	Au etchant
			Time	About 1 min
5, 11, 15	Resist removal	Acetone	Time	5 min
6	PEDOT deposition		Thickness	160 nm
		Spin coater	Spin coating	1st 500 rpm/5 sec
				2nd 1500 rpm/35 sec
		Hot plate	Baking	75℃/20 min
7	Insulating layer deposition	Parylene deposition apparatus	Dimer	Parylene C
			Dimer amount	3.42 (6.84) g
12	RIE etching	RIE machine	Power	200 W
			Gas/ flow rate	O_2/30 sccm
			Pressure	0.05 Torr
			Time	2 (4) min

Table 5.2. Fabrication process conditions of the micro-potentiometer mounted on the flexible slider (continued).

No	Process steps	Equipment/ process	Conditions	
16	μpools structure SU-8 Photolithography		Resist	SU-8 3050
		Spin coater	Spin coating	1st slope/10 sec
				2nd 1000 rpm/10 sec
				3rd slope /10 sec
				4th 2000 rpm/70 sec
		Hot plate	Pre-baking	65℃/5 min; 95℃/15 min
		Mikasa Exposure Machine	Exposure time	35 sec
			UV intensity	9.2 mJ/cm^2
		Hot plate	Post baking	95℃/15 min
		Developing solution (SU-8 Developer)	Development	5 min
		Hot plate	Hard baking	95℃/1 min
17	Laser cutting	Excimer laser	Output	4.8 mJ
18	Conductive liquid filling	Syringe		Conductive liquid
19	Mechanical peel off			

The fabricated slider is shown in Figure 5.6(*b*) with its dimensions listed in Table 5.3. We evaluated the sensitivity and resolution of the fabricated micro-potentiometer. As mentioned above (Figure 5.5), the sensing principle of the micro-potentiometer relied on the variability of the relative resistance Z between the two probes. The relative resistance changes in direct proportion to the displacement of the slider. The micro-potentiometer was mounted on the slider, and two probes were dipped into two μpools filled with the ionic liquid. The relative resistance between two probes was measured at different positions of the slider using a LCR meter. Figure 5.7 shows the resistance with

Table 5.3. Dimension of the fabricated micro-potentiometer.

L(mm)	W (mm)	H (μm)	l (μm)	w_e (μm)	w_s (μm)	h (μm)
25	5	5	3500	600	500	40

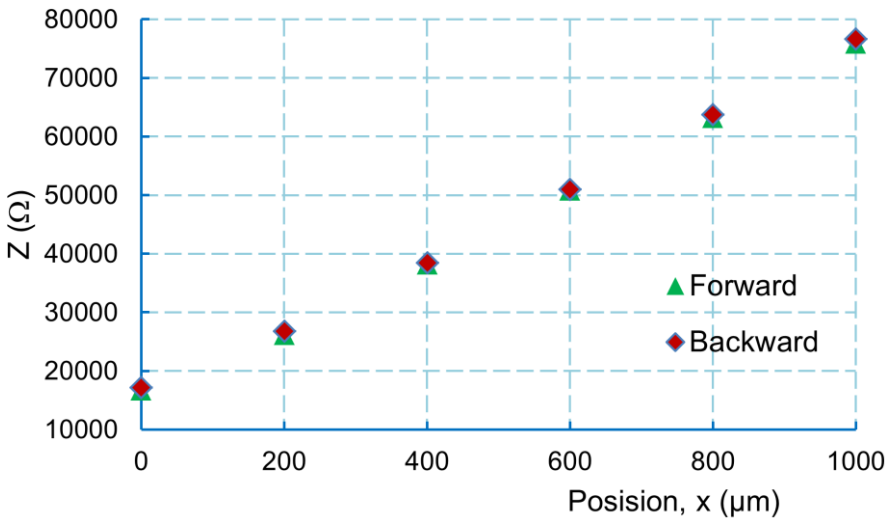

Figure 5.7. The measured resistance of the micro-potentiometer using a LCR meter at 10 kHz.

respect to the displacement of the slider in the forward and backward motion. The initial resistance is determined by the resistance between the two probes at the initial position of the slider. We calculated the sensitivity and resolution of the micro-potentiometer on the basis of those measured values.

The sensitivity A is expressed as

$$A = \frac{\Delta Z}{\Delta X} \tag{5.6}$$

where ΔZ is the change of the resistance of the micro-potentiometer in the travel range of the slider ΔX.

The resolution B obtains by dividing the maximum standard deviation value $s_{max}(x)$ from the sensitivity A

$$B = \frac{s_{\max}(x)}{A} \tag{5.7}$$

The standard deviation value in each position of the slider is

$$s(x) = \sqrt{\frac{1}{n}\sum_{i=1}^{n}\left(Z_i(x) - \overline{Z}(x)\right)^2} \tag{5.8}$$

where $Z_i(x)$ is the output value of the micro-potentiometer at position i; n is the total measured position; $\overline{Z}(x)$ is the average output value

$$\overline{Z}(x) = \frac{1}{n}\sum_{i=1}^{n} Z_i(x) \tag{5.9}$$

From the experimental results as shown in Figure 5.7, the sensitivity of the fabricated micro-potentiometer was 62 Ω μm^{-1}, and the resolution was 6 μm. We also evaluated the sensitivity of the micro-potentiometer corresponding to the ECLIA control system. The sensitivity was 0.77 mV μm^{-1} in this situation.

5.3. Results and discussions of ECLIA feedback control

5.3.1. Characteristics of stepwise motion

In this section, we investigate the stepwise motion of the slider. As mentioned above, the slider motion was driven by the motion of the PZT actuator combined with an electrostatic clutch mechanism. The stepping displacement depends on the applied voltage and driving frequency. The higher voltage produces the larger displacement; otherwise, the higher driving frequency generates the smaller displacement due to the hysteresis and creep behaviors of the PZT actuator. The electrostatic clutch mechanism is affected by the electrostatic force. The higher applied voltage performs the better clutch; however, this electrostatic clutch structure may cause the relative sliding between the slider and the contact electrode.

Experiments were carried out to investigate the characteristics of the slider motion. The voltage applied to the PZT actuator and to the slider was 30 V at which the electrostatic clutch mechanism worked properly. To demonstrate the stepwise displacement, we operate the slider moving a displacement d of 110 μm with certain driving frequencies f of 1, 10, and 100 Hz. If the duration of control time corresponding with each frequency is T, the number of steps n can be defined as

$$n = fT \tag{5.10}$$

The mean value of the stepwise length s is calculated on the basis of the displacement d and the number of steps n using

$$s = \frac{d}{n} \tag{5.11}$$

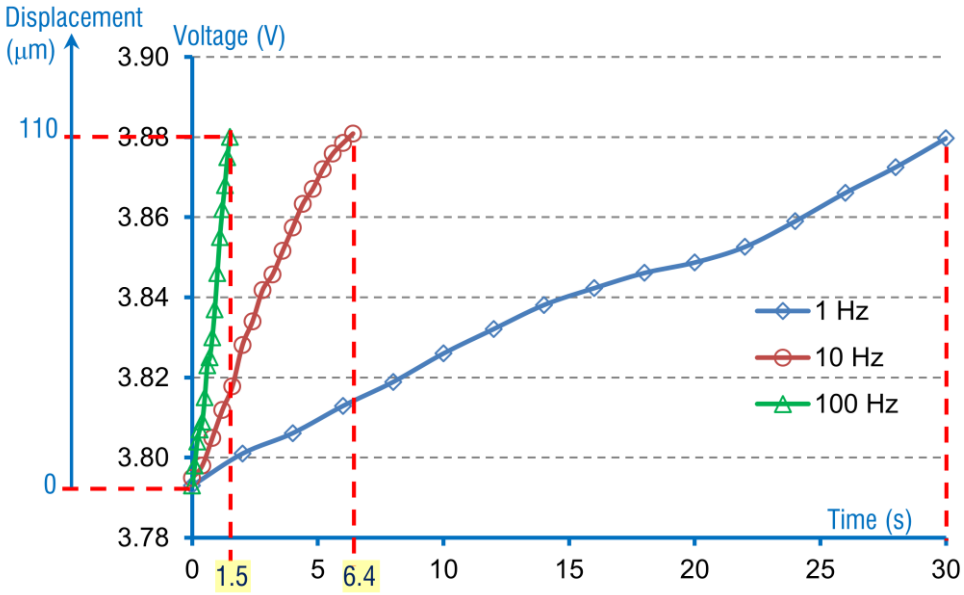

Figure 5.8. Time courses of the slider displacements at different driving frequencies.

The micro-potentiometer and corresponding data circuit were utilized to acquire the slider position. Figure 5.8 shows the measured displacements of the slider at different frequencies. The vertical axis represents the acquired voltage from the micro-potentiometer that corresponds to the slider displacement; the horizontal axis is the time course. Under this condition, the mean stepwise lengths of the slider at 1, 10, and 100 Hz were 3.67, 1.73, and 0.74 μm, respectively. These results indicated that the electrostatic clutch mechanism was unstable. The stepping displacement varied with each step and decreased when the driving frequency increased.

5.3.2. Preliminary evaluation of tuning gains

As discussed in previous section, the stepwise motion of the slider varied with each step and was affected by the applied voltages, driving frequency, clutch mechanism, etc. These phenomena cause the difficulty in building a mathematical model of the ECLIA system. Therefore, we use the ECLIA system to investigate the tuning gains for the feedback controller. In this section, we evaluate the specific factors of the ECLIA that influence the tuning gains.

The PI controller using the tuning parameters automatically adjusts the driving frequency of applied voltage to the ECLIA. Tuning parameters affect the response time, overshoot and steady state of the system. The stepwise motion of the slider is operated by the motion of the PZT actuator combined with the electrostatic clutch mechanism

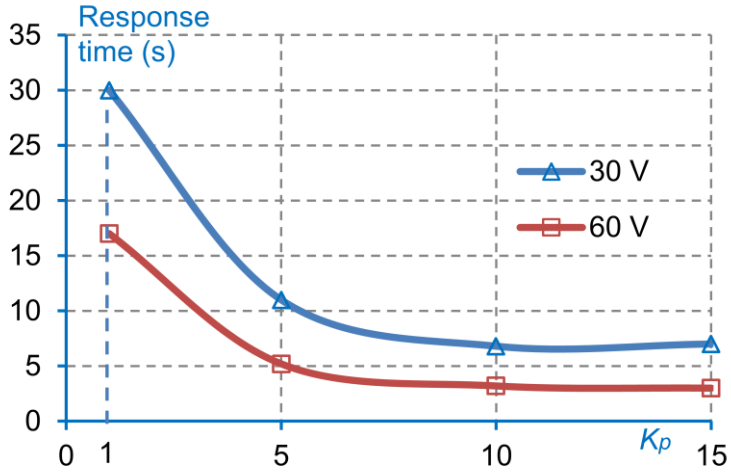

Figure 5.9. Response times at different tuning gains K_p and applied voltages.

that is driven by applied voltages. Higher voltages generate larger stepwise motion of the slider and allow choosing the smaller tuning gains. Additionally, the higher driving frequency also causes larger relative sliding of the clutch mechanism. If the driving frequency increases to a certain value, the motion of the PZT actuator cannot transfer to the slider. Consequently, the applied voltages and driving frequency are important factors that influence the stepwise motion of the slider and the selection of tuning gains. These considerations are investigated in the following section.

5.3.3. System response

We developed a PI feedback control system for the ECLIA, which was discussed above. This feedback control was investigated to find reasonable tuning gains and to test the performance of the ECLIA control system. Figure 5.10 shows the experimental control responses with the forward motion of the slider at different tuning gains. The system response without tuning gains was also investigated and compared to that with the PI feedback controller. The initial position had a digital value of 770 (3,760 mV), and the reference position was 820 (4,004 mV), which corresponded to a 317 μm ((4,004 mV – 3,760 mV) / 0.77 mV μm^{-1}) displacement of the slider under this condition.

The red curve in Figure 5.10 describes the ECLIA response without tuning gains (K_p = 0 and K_i = 0) at a frequency of 100 Hz. The control signal with this constant frequency drives the slider with constant velocity. The results show that there was an overshoot and oscillation with a peak of 21 μm (338 μm – 317 μm). The rise time is rather short (4 s), whereas the settling time is approximately three times longer (11 s).

This indicates that the high-frequency control signal at 100 Hz caused vibration in the slider, resulting in the instability of the electrostatic clutch mechanism and taking a long time to approach the steady state. As mentioned above, the feedback controller uses the tuning gains to generate the driving voltage with the gradual reduction of frequency to the ECLIA. This means that the velocity of the slider reduces gradually when approaching to the target position. It intends to reduce control time, overshoot, and oscillation.

A simple control system is first considered with only the proportional gain K_p (K_i = 0). The system response is investigated by changing tuning gain values. The ECLIA system works properly at tens of hertz of the driving frequency. We selected K_p = 1 at which the initial driving frequency (at the starting time of the control process) was approximately 15 Hz in this condition. As discussed above, a voltage of 30 V was applied to the PZT actuator and the clutch mechanism. The blue curve in Figure 5.9 shows the response time with respect to the different tuning gains K_p. The response times decreased by approximately 70 %, from 30 to 11 s when K_p changed from 1 to 5. However, it reduced by 35 %, from 11 to 7 s with the increase of K_p from 5 to 10. It was almost no additional decrease when K_p changed from 10 to 15. These indicate that relative sliding of the clutch mechanism caused the limited reduction of the response time. The clutch mechanism was unstable when the driving frequency was higher than

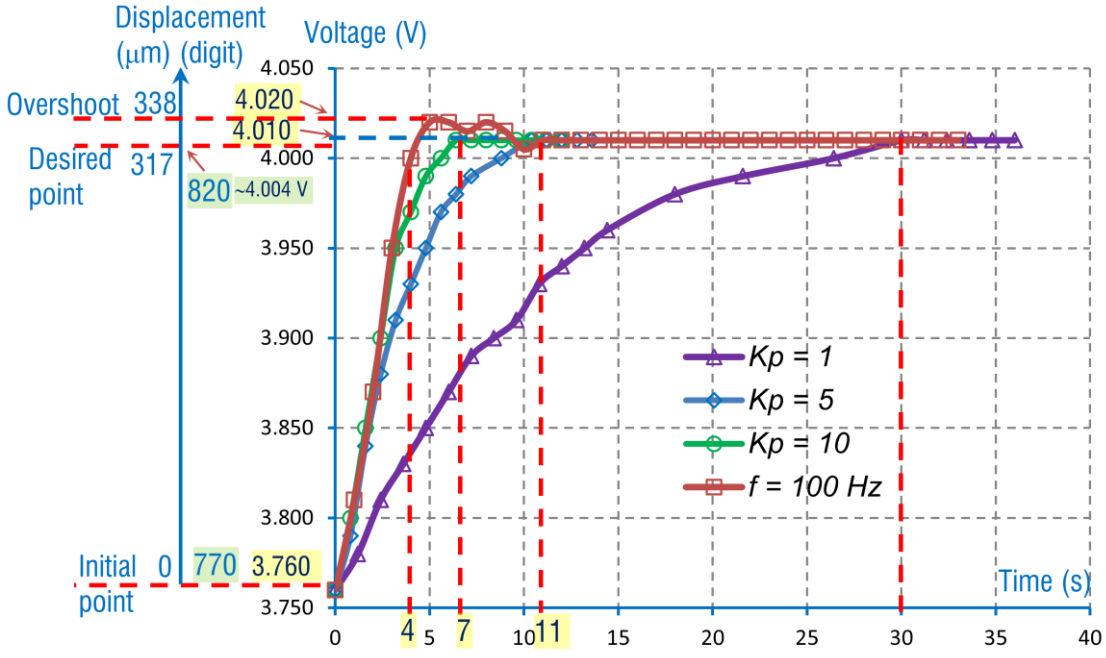

Figure 5.10. ECLIA system response at different values of K_p and at a frequency of 100 Hz

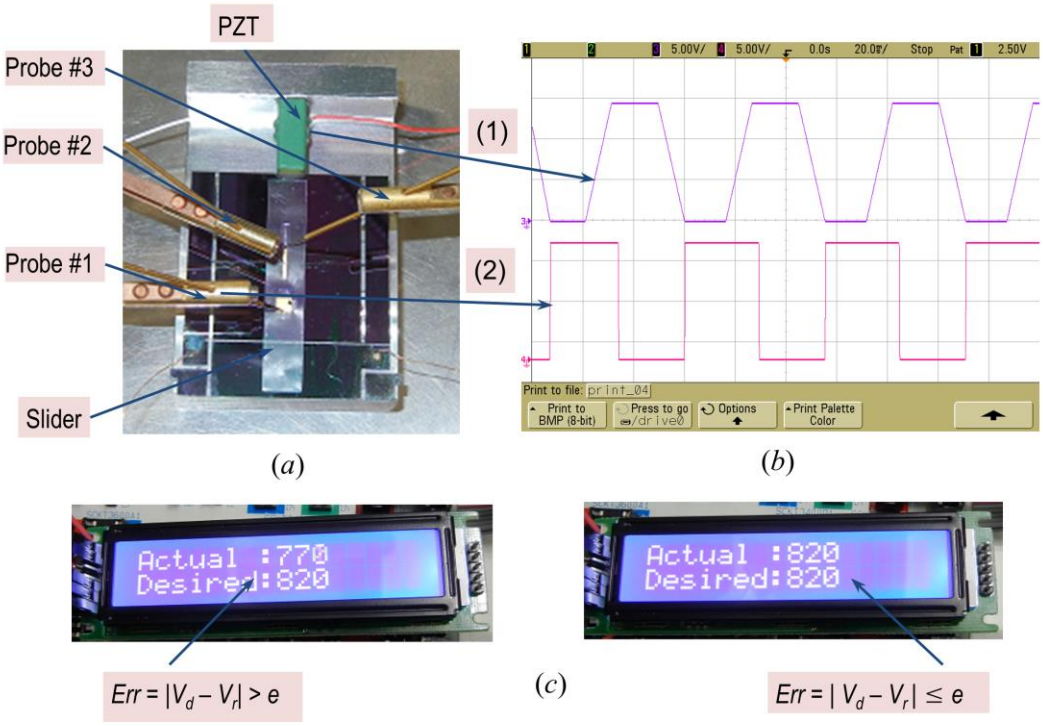

Figure 5.11. Images of (*a*) ECLIA system, (*b*) output control signals for the PZT actuator (1) and slider (2), and (*c*) LCD monitor to display the actual and desired positions of the slider.

120 Hz in this situation. The higher applied voltage generated the larger motion of the PZT actuator, and the better electrostatic clutch mechanism. Thus, the tuning gain K_p was also considered at a voltage of 60 V. The red curve in Figure 5.9 shows that the response times at various K_p corresponding to 60 V reduced by approximately 50 % comparing with that of 30 V. The changing rate of the response time was quite similar in both cases, and the stepwise motion of the slider was proportional to the applied voltage. Taking these considerations into account, K_p can be chosen with the suitability of the response time and applied voltages in practical use.

Figure 5.10 shows the system response at different tuning gains K_p corresponding to the voltage of 30 V. We can observe that there was no overshoot, oscillation, and the steady state was stable in these situations. Hence, the adjustment of K_i in this condition was not necessary. The steady-state error of the slider, which is defined as the difference between the desired value V_d = 820 (4,004 mV) and the measured value (4,010 mV), is approximately 8 μm ((4,010 mV – 4,004 mV) / 0.77 mV μm^{-1}) corresponding to 2.5 % of the steady-state value. It is acceptable in practical use. This error is caused by the sensitivity and resolution of the micro-potentiometer, and the accuracy of the ADC module.

5.3.4. Slider manipulation

By using the feedback control with selected tuning gain of K_p = 10 for short control time, Figure 5.11(*a*) shows the ECLIA system for operating a slider to the desired position with a setting error *e* of 0. Probe #1 supplies an electrical signal to the slider. Probe #2 and probe #3 are the sensing probes of the micro-potentiometer. An oscilloscope was utilized to monitor the output analog signals for the PZT actuator (1) and slider (2) (Figure 5.11(*b*)). An LCD monitor displayed the desired and actual positions of the slider in digital values (Figure 5.11 (*c*)). The desired position of the slider V_d was 820. The current position of the slider displayed on the upper monitor V_{r1} was 770. The current error Err_1 (Err_1 = |820 – 770| = 50) was larger than the setting error *e*. Therefore, output signals (Figure 5.11 (*b*)) were generated to control the forward movement of the slider until the slider reached the desired position, with the lower monitor in Figure 5.11 (*c*) (Err_2 = 0) showing that the actual position was equal to the desired position. The slider was moved successfully to the desired position.

5.3.5. Discussions

In this chapter, a feedback control for the ECLIA was introduced and demonstrated. The stepwise displacement of the slider varied with each step and also decreased as the increase in driving frequency. These characteristics were caused by the inherent hysteresis and creep phenomena of the PZT actuator, and the instability of the electrostatic clutch mechanism. The tuning gains are evaluated on the basis of the applied voltage, driving frequency, and clutch mechanism. The feedback control exhibits no overshoot and oscillation when adjusting various tuning gains. The high performance of the position feedback control aims future applications of the ECLIA.

The buckling force of the fishbone slider (cross section of the backbone as 300 μm × 80 μm) of 5 mN could meet the pushing force requirement of micro-syringe pumps that requires sub-mN for direct liquid manipulation [50]. The pushing force requirement is the reaction force of liquid in the micro-channel that is estimated by surface tension of liquid on the wall of micro-channel. The pushing force of 0.12 mN is calculated from the cross section of the micro-channel (320 μm × 100 μm) and surface tension of water of 71.97 mN m^{-1}. The feedback controller allows gradual decrease in velocity of the slider that achieves several steps per second when approaching the desired position. This characteristic allows the picoliter-per-second range of liquid dispenser in the micro-channel that could satisfy the minimal overflow of liquid manipulation for micro-syringe pumps application. The flow of liquid (118 pL s^{-1}) is

estimated on the basis of the velocity of the slider at the driving frequency of 1 Hz (3.67 μm s^{-1}) as stated in the section 5.3.1.

5.4. Summary

We have successfully designed and implemented a feedback control using a micro-potentiometer and microcontroller as a development stage for the ECLIA. The tuning parameters, which were affected by the applied voltages, driving frequency and stepwise motion, have been investigated. The system response at a higher driving frequency of 100 Hz prompted an overshoot and oscillation. The feedback controller, that automatically adjusts the frequency of the driving voltage, showed a significant improvement compared to a closed-loop control without tuning gains. The slider was moved successfully to the desired position with faster control time, no overshoot, oscillation, and a steady-state error of 8 μm (~ 2.5 %).

In future work, the ECLIA feedback control will be applied for micro-syringe pumps. The characteristics of feedback control that mention in the discussions section aim to improve the performance of micro-syringe pumps.

Chapter 6

CONCLUSIONS

In this thesis, we aim to improve the performance of an electrostatically controlled linear actuator (ECLIA) as its development stage. The ECLIA generates precise stepwise motion, large travel range and independence of multiple sliders via a PZT actuator and an electrostatic clutch mechanism. However, the air gap causes lower efficiency of the electrostatic and pushing-force generation of sliders. Relative sliding of the electrostatic clutch mechanism affects the position control of the actuator. The main objective of this research is to enhance electrostatic, pushing forces of the slider and position feedback control for high performance of the ECLIA.

We evaluated the characteristics of stepwise motion on the basis of the ECLIA model. The results show that the stepwise length of the slider is inequality due to the instability of the electrostatic clutch mechanism, and the creep behavior and inherent hysteresis of the PZT actuator. To reduce the air gap for improving electrostatic-force generation, we proposed the flexible electrode that consists of a PEDOT conductive layer sandwiched between insulating parylene layers. Different materials were evaluated to optimize the selection of materials for the electrode. The characteristics such as air gap, capacitance, and electrostatic force were investigated to compare the performance between the PEDOT-parylene electrode and the Si electrode. The electrostatic clutching force between the PEDOT-parylene and Si electrodes at 30 V was approximately that between two Si electrodes at 100 V. The PEDOT-parylene electrode is employed as the flexible slider for the ECLIA. The flexible slider achieved higher electrostatic force generation. But, it has lower longitudinal stiffness and produces smaller pushing force. We proposed a fishbone structure mounted on the PEDOT-parylene slider to improve pushing-force generation for the slider. The buckling force of the fishbone slider was 5 mN that achieved much significantly with 166 times larger than that of the flexible slider (0.03 mN). The pushing force of the fishbone slider performed higher improvement with three times larger than the Si slider. This pushing force is sufficient for most applications of the ECLIA. We also designed and implemented a position feedback control using a micro-potentiometer and microcontroller for the

ECLIA. The tuning gains were evaluated on the basis of the applied voltage, driving frequency, and clutch mechanism. The system response prompted an overshoot and oscillation at a higher driving frequency of 100 Hz. The feedback controller, that automatically adjusts the frequency of the driving voltage, showed a significant improvement compared to a closed-loop control without tuning gains. The slider was moved successfully to the desired position with faster control time, no overshoot, oscillation, and a steady-state error of 8 μm (~ 2.5 %).

In future work, the fabrication method will be improved to obtain the thinner slider for higher efficiency of electrostatic clutching force. The rigid of the fishbone structure should be increased to have higher pushing-force generation. The ECLIA feedback control will be applied for micro-syringe pumps. The characteristics of feedback control aim to improve the performance of micro-syringe pumps.

BIBLIOGRAPHY

[1] Erismis M ., Neves H P, Puers R and Van Hoof C 2008 A Low-Voltage Large-Displacement Large-Force Inchworm Actuator *J. Microelectromechanical Syst.* **17** 1294–301

[2] De Boer M P, Luck D L, Ashurst W R, Maboudian R, Corwin A D, Walraven J . and Redmond J M 2004 High-performance surface-micromachined inchworm actuator *J. Microelectromechanical Syst.* **13** 63–74

[3] Tas N, Wissink J, Sander L, Lammerink T and Elwenspoek M 1998 Modeling, design and testing of the electrostatic shuffle motor *Sens. Actuators Phys.* **70** 171–8

[4] Geisberger A, Sarkar N, Ellis M and Skidmore G D 2003 Electrothermal properties and modeling of polysilicon microthermal actuators *J. Microelectromechanical Syst.* **12** 513–23

[5] Sinclair M J 2000 A high force low area MEMS thermal actuator *The Seventh Intersociety Conference on Thermal and Thermomechanical Phenomena in Electronic Systems, 2000. ITHERM 2000* The Seventh Intersociety Conference on Thermal and Thermomechanical Phenomena in Electronic Systems, 2000. ITHERM 2000 vol 1 p -132

[6] Konishi S, Ohno K and Munechika M 2002 Parallel linear actuator system with high accuracy and large stroke *Sens. Actuators Phys.* **97–98** 610–9

[7] Changhai R and Lining S 2005 Hysteresis and creep compensation for piezoelectric actuator in open-loop operation *Sens. Actuators Phys.* **122** 124–30

[8] Lining S, Changhai R, Weibin R, Liguo C and Minxiu K 2004 Tracking control of piezoelectric actuator based on a new mathematical model *J. Micromechanics Microengineering* **14** 1439

[9] Haddab Y, Chaillet N and Bourjault A 2000 A microgripper using smart piezoelectric actuators *2000 IEEE/RSJ International Conference on Intelligent Robots and Systems, 2000. (IROS 2000). Proceedings* 2000 IEEE/RSJ International Conference on Intelligent Robots and Systems, 2000. (IROS 2000). Proceedings vol 1 pp 659–64 vol.1

[10] Böhm S, Burger G J, Korthorst M T and Roseboom F 2000 A micromachined silicon valve driven by a miniature bi-stable electro-magnetic actuator *Sens. Actuators Phys.* **80** 77–83

[11] Wright J A, Tai Y-C and Chang S-C 1997 A large-force, fully-integrated MEMS magnetic actuator , *1997 International Conference on Solid State Sensors and Actuators, 1997. TRANSDUCERS '97 Chicago* , 1997 International Conference on

Solid State Sensors and Actuators, 1997. TRANSDUCERS ’97 Chicago vol 2 pp 793–6 vol.2

[12] Sendoh M, Ishiyama K and Arai K-I 2003 Fabrication of magnetic actuator for use in a capsule endoscope *IEEE Trans. Magn.* **39** 3232–4

[13] Jeong O C and Konishi S 2008 The self-generated peristaltic motion of cascaded pneumatic actuators for micro pumps *J. Micromechanics Microengineering* **18** 085017

[14] Konishi S, Kawai F and Cusin P 2001 Thin flexible end-effector using pneumatic balloon actuator *Sens. Actuators Phys.* **89** 28–35

[15] Bütefisch S, Seidemann V and Büttgenbach S 2002 Novel micro-pneumatic actuator for MEMS *Sens. Actuators Phys.* **97–98** 638–45

[16] Kondo S, Yoshimura S-I, Saito N, Tanioka K and Esashi M 2001 Precise control of small displacements of a stacked piezoelectric actuator by means of layer-by-layer driving *The 14th IEEE International Conference on Micro Electro Mechanical Systems (MEMS 2001)* pp 248–51

[17] Yamanishi Y, Sakuma S and Arai F 2007 Magnetically Modified Soft Micro Actuators for Oocyte Manipulation *International Symposium on Micro-NanoMechatronics and Human Science, 2007. MHS ’07* International Symposium on Micro-NanoMechatronics and Human Science, 2007. MHS ’07 pp 442–7

[18] Chronis N and Lee L P 2005 Electrothermally Activated SU-8 Microgripper for Single Cell Manipulation in Solution *J. Microelectromechanical Syst.* **14** 857–63

[19] Lopez-Sanchez J, Miribel-Catala P, Montane E, Puig-Vidal M, Bota S A, Samitier J, Simu U and Johansson S 2001 High accuracy piezoelectric-based microrobot for biomedical applications *2001 8th IEEE International Conference on Emerging Technologies and Factory Automation, 2001. Proceedings* 2001 8th IEEE International Conference on Emerging Technologies and Factory Automation, 2001. Proceedings vol 2 pp 603–9 vol.2

[20] Carrozza M C, Eisinberg A, Menciassi A, Campolo D, Micera S and Dario P 2000 Towards a force-controlled microgripper for assembling biomedical microdevices *J. Micromechanics Microengineering* **10** 271–6

[21] Cusin P, Sawai T and Konishi S 2000 Compact and precise positioner based on the Inchworm principle *J. Micromechanics Microengineering* **10** 516

[22] Mita M, Arai M, Tensaka S, Kobayashi D, Basset P, Kaiser A, Masquelier P, Buchaillot L, Collard D and Fujita H 2001 Electrostatic impact-drive microactuator *The 14th IEEE International Conference on Micro Electro Mechanical Systems (MEMS 2001)* pp 590–3

[23] Sahu B, Taylor C R and Leang K K 2010 Emerging Challenges of Microactuators for Nanoscale Positioning, Assembly, and Manipulation *J. Manuf. Sci. Eng.* **132** 030917–030917

[24] Akiyama T and Shono K 1993 Controlled stepwise motion in polysilicon microstructures *J. Microelectromechanical Syst.* **2** 106–10

[25] Konishi S, Oshima A, Kinoshita N, Kumagaya I, Kishi T, Shimazu T and Katayama M 2005 Batch-fabricated high dense multi sliders for WDM spectral attenuation *The 13th International Conference on Solid-State Sensors, Actuators and Microsystems, 2005. Digest of Technical Papers. TRANSDUCERS '05* vol 2 pp 1242–5

[26] Yokokawa R, Saika T, Nakayama T, Fujita H and Konishi S 2006 On-chip syringe pumps for picoliter-scale liquid manipulation *Lab. Chip* **6** 1062–6

[27] Seidemann V, Bütefisch S and Büttgenbach S 2002 Fabrication and investigation of in-plane compliant SU8 structures for MEMS and their application to micro valves and micro grippers *Sens. Actuators Phys.* **97–98** 457–61

[28] Millet O, Bernardoni P, Régnier S, Bidaud P, Tsitsiris E, Collard D and Buchaillot L 2004 Electrostatic actuated micro gripper using an amplification mechanism *Sens. Actuators Phys.* **114** 371–8

[29] Ito M, Kuwamura T, Komoda J and Konishi S 2011 Conductive polymer coated flexible electrode for highly efficient force generation of electrostatic actuator *The 24th IEEE International Conference on Micro Electro Mechanical Systems (MEMS2011)* pp 392–5

[30] Ito M, Maeda T, Simizu K and Konishi S 2009 Minimally restricted wiring by probe dipping micro-pool (PDP) connection *Proc. of National Conference of IEEJ2009, Sapporo, Japan*

[31] Ito M, Kuwamura T and Konishi S 2010 Low physical restriction MEMS potentiometer using probe dipping micro-pool with conductive liquid *The 23rd IEEE International Conference on Micro Electro Mechanical Systems (MEMS2010)* pp 288–91

[32] Mukaro R and Carelse X F 1999 A microcontroller-based data acquisition system for solar radiation and environmental monitoring *IEEE Trans. Instrum. Meas.* **48** 1232–8

[33] Koizumi H, Mizuno T, Kaito T, Noda Y, Goshima N, Kawasaki M, Nagasaka K and Kurokawa K 2006 A Novel Microcontroller for Grid-Connected Photovoltaic Systems *IEEE Trans. Ind. Electron.* **53** 1889–97

[34] Huang H-P, Jeng J-C, Chiang C-H and Pan W 2003 A direct method for multi-loop PI/PID controller design *J. Process Control* **13** 769–86

[35] Toscano R 2005 A simple robust PI/PID controller design via numerical optimization approach *J. Process Control* **15** 81–8

[36] Chen D and Seborg D E 2002 PI/PID Controller Design Based on Direct Synthesis and Disturbance Rejection *Ind. Eng. Chem. Res.* **41** 4807–22

[37] Saika T 2007 *Study on electrostatically controlled linear actuator (ECLIA) and its application to micro-syringe* (Ritsumeikan University)

[38] Howell L L 2001 *Compliant Mechanisms* (John Wiley & Sons)

[39] Takeuchi S, Ziegler D, Yoshida Y, Mabuchi K and Suzuki T 2005 Parylene flexible neural probes integrated with microfluidic channels *Lab. Chip* **5** 519–23

[40] Rapp B E, Voigt A, Dirschka M and Länge K 2012 Deposition of ultrathin parylene C films in the range of 18 nm to 142 nm: Controlling the layer thickness and assessing the closeness of the deposited films *Thin Solid Films* **520** 4884–8

[41] Petroni S, Tegola C L, Caretto G, Campa A, Passaseo A, Vittorio M D and Cingolani R 2011 Aluminum Nitride piezo-MEMS on polyimide flexible substrates *Microelectron. Eng.* **88** 2372–5

[42] Xiao S Y, Che L F, Li X X and Wang Y L 2008 A novel fabrication process of MEMS devices on polyimide flexible substrates *Microelectron. Eng.* **85** 452–7

[43] Yasufuku S 1995 Application of aramid film to electrical and electronic uses in Japan *IEEE Electr. Insul. Mag.* **11** 27–33

[44] Hong W, Xu Y, Lu G, Li C and Shi G 2008 Transparent graphene/PEDOT–PSS composite films as counter electrodes of dye-sensitized solar cells *Electrochem. Commun.* **10** 1555–8

[45] Greczynski G, Kugler T and Salaneck W R 1999 Characterization of the PEDOT-PSS system by means of X-ray and ultraviolet photoelectron spectroscopy *Thin Solid Films* **354** 129–35

[46] Ryu K S, Hong Y-S, Park Y J, Wu X, Kim K M, Lee Y-G, Chang S H and Lee S J 2004 Polyaniline doped with dimethylsulfate as a polymer electrode for all solid-state power source system *Solid State Ion.* **175** 759–63

[47] Ramanavičius A, Ramanavičienė A and Malinauskas A 2006 Electrochemical sensors based on conducting polymer—polypyrrole *Electrochimica Acta* **51** 6025–37

[48] Mukaro R and Carelse X F 1999 A microcontroller-based data acquisition system for solar radiation and environmental monitoring *IEEE Trans. Instrum. Meas.* **48** 1232–8

[49] Koizumi H, Mizuno T, Kaito T, Noda Y, Goshima N, Kawasaki M, Nagasaka K and Kurokawa K 2006 A Novel Microcontroller for Grid-Connected Photovoltaic Systems *IEEE Trans. Ind. Electron.* **53** 1889–97

[50] Nguyen T A and Konishi S 2014 Characterization of sliders for efficient force generation of electrostatically controlled linear actuator *J. Micromechanics Microengineering* **24** 055012